Performance, Facility Pressure Effects, and Stability Characterization Tests of NASA's Hall Effect Rocket with Magnetic Shielding Thruster

Hani Kamhawi[1], Wensheng Huang[2], Thomas Haag [3], John Yim[4], and Daniel Herman[5]
NASA Glenn Research Center, Cleveland, OH, 44135, USA

Peter Y. Peterson[6]
Vantage Partners, LLC
NASA Glenn Research Center, Cleveland, OH, 44135, USA

George Williams[7], and James Gilland[8]
Ohio Aerospace Institute
NASA Glenn Research Center, Cleveland, OH, 44135, USA

Richard Hofer[9] and Ioannis Mikellides[10]
Jet Propulsion Laboratory, California Institute of Technology, Pasadena, CA, 91109, USA

NASA's Hall Effect Rocket with Magnetic Shielding (HERMeS) 12.5 kW Technology Demonstration Unit-1 (TDU-1) has been the subject of extensive technology maturation in preparation for flight system development. Part of the technology maturation effort included experimental evaluation of the TDU-1 thruster with conducting and dielectric front pole cover materials in two different electrical configurations. A graphite front magnetic pole cover thruster configuration with the thruster body electrically tied to cathode, and an alumina front pole cover thruster configuration with the thruster body floating were evaluated. Both configurations were also evaluated at different facility background pressure conditions to evaluate background pressure effects on thruster operation. Performance characterization tests found that higher thruster performance was attained with the graphite front pole cover configuration with the thruster electrically tied to cathode. A total thrust efficiency of 68% and a total specific impulse of 2,820 s was demonstrated at a discharge voltage of 600 V and a discharge power of 12.5 kW. Thruster stability regimes were characterized with respect to the thruster discharge current oscillations and with maps of the discharge current-voltage-magnetic field (IVB). Analysis of TDU-1 discharge current waveforms found that lower normalized discharge current peak-to-peak and root mean square magnitudes were attained when the thruster was electrically floated with alumina front pole covers. Background pressure effects characterization tests indicated that the thruster performance and stability were mostly invariant to changes in the facility background pressure for vacuum chamber pressure below 1×10^{-5} Torr-Xe (for thruster flow rates of 20.5 mg/s). Power spectral density

---

[1] Senior Research Engineer, Electric Propulsion Systems Branch, AIAA Associate Fellow.
[2] Research Engineer, Electric Propulsion Systems Branch, AIAA Senior Member.
[3] Senior Research Engineer, Electric Propulsion Systems Branch, AIAA Senior Member.
[4] Research Engineer, Electric Propulsion Systems Branch, AIAA Senior Member.
[5] Research Engineer, Electric Propulsion Systems Branch, AIAA Senior Member.
[6] Senior Research Engineer, Electric Propulsion Systems Branch, AIAA Senior Member.
[7] Principle Scientist, Electric Propulsion Systems Branch, AIAA Associate Fellow.
[8] Research Team Manager, Electric Propulsion Systems Branch, AIAA Associate Fellow.
[9] Senior Engineer, Electric Propulsion Group, AIAA Associate Fellow.
[10] Senior Engineer, Electric Propulsion Group, AIAA Associate Fellow.

analysis of the discharge current waveforms showed that increasing the vacuum chamber background pressure resulted in a higher discharge current dominant breathing mode frequency. Finally, IVB maps of the TDU-1 thruster indicated that the discharge current became more oscillatory with higher discharge current peak-to-peak and RMS values with increased facility background pressure at lower thruster mass flow rates; thruster operation at higher flow rates resulted in less change to the thruster's IVB characteristics with elevated background pressure.

I. Introduction

For missions beyond low Earth orbit, spacecraft size and mass can be dominated by onboard chemical propulsion systems and propellants that may constitute more than 50 percent of the spacecraft mass. This impact can be substantially reduced through the utilization of Solar Electric Propulsion (SEP) due to its substantially higher specific impulse. Studies performed for NASA's Human Exploration and Operations Mission Directorate and Science Mission Directorate have shown that a 50-kW-class SEP capability can be enabling for both near term and future architectures and science missions. To enable SEP missions at the power levels required for these applications, an in-space demonstration of an operational 50-kW-class SEP spacecraft has been proposed as an SEP Technology Demonstration Mission (TDM).[1] In 2010, NASA's Space Technology Mission Directorate (STMD) began developing large, deployable photovoltaic solar array structures for high-power electrical power production and high-power electric propulsion technologies.[2,,,7] The maturation of these critical technologies has made mission concepts utilizing high-power SEP viable.

The Asteroid Redirect Robotic Mission (ARRM) is the leading candidate for SEP TDM concepts that utilizes an SEP spacecraft to return up to 20 metric tons (up to 6 m maximum extent) of asteroidal mass from the surface of a larger asteroid, to a stable orbit around the Moon for subsequent access by a human crewed mission.[8,9,10,11,12] The Ion Propulsion System (IPS) for ARRM will be used for heliocentric transfer from Earth to the target asteroid, orbit capture at the asteroid, transfer to a low orbit about the asteroid, a planetary defense demonstration after retrieval of the asteroidal mass from the larger asteroid, departure and escape from the asteroid, heliocentric transfer from the asteroid to lunar orbit, and insertion into a lunar distant retrograde orbit. In addition, the IPS will provide pitch and yaw control of the spacecraft during IPS thrusting. To date, the technology development, performed by the NASA Glenn Research Center (GRC) and the Jet Propulsion Laboratory (JPL), has been focused on an in-house effort to mature the high-power Hall thruster and power processing designs. This work had recently begun the transition to a commercial vendor for the development of an Engineering Development Unit (EDU) electric propulsion (EP) string and optional Qualification Model (QM) and Flight Model (FM) hardware delivery in a timeline consistent with the current ARRM implementation. The flight electric propulsion string hardware will be provided as government furnished equipment to the Asteroid Redirect Vehicle (ARV) prime contractor.

The NASA GRC and JPL team are continuing the development of NASA's Hall Effect Rocket with Magnetic Shielding (HERMeS). Two Technology Demonstration Units (TDU-1 and TDU-2) have been fabricated and are being subjected to testing in a series of parallel efforts that are planned to increase the Technology Readiness Level (TRL).

Tests of TDU-1 were initiated in 2015.[13] Tests included performance characterization, thermal characterization, magnetic shielding verification, abbreviated stability evaluation, and a preliminary assessment of pressure facility effects on the thruster operation. TDU-1 performance tests performed in 2015 demonstrated thruster total efficiency above 60% and total specific impulse of 3,000 s for the thruster operating at a discharge voltage of 800 V and a discharge power of 12.5 kW [9]. Thermal characterization tests indicated that for thruster operation at 800 V and 12.5 kW, peak thruster temperatures were within the prescribed maximum material temperature limits. The thruster's magnetic shielding was confirmed using Langmuir probes embedded in the discharge channel walls; a plasma potential of 800 V was measured along the entire length of the inner and outer discharge channel walls.[14] The magnetic shielding test on TDU-1 verified that channel erosion was no longer expected to limit the life of the thruster. Pressure effects testing on the TDU-1 thruster found that the thruster performance was mostly invariant to increased facility background pressure. Finally, the 2015 TDU-1 test campaign, although very successful, identified magnetic front pole erosion as the potential next life limiting phenomenon that needs to be addressed for the TDU-1 thruster design. Results from the thermal characterization test and the uncovering of the front pole erosion as a potential life limiting phenomenon required that design modifications be implemented on the TDU-1 and TDU-2 thruster design.

II. Background

Tests of TDU-1 in 2015 indicated that design changes were required to increase the thermal margin of the thruster and to protect the thruster front poles from erosion due to ion bombardment. Two design changes were implemented to TDU-1 including:

1. Improved mechanical contact between the propellant manifold/discharge channel and the magnetic backpole. This improved contact increased the thermal conduction to the radiator and reduced the temperatures of the internal components; and

2. Installation of front pole covers to protect the front magnetic circuit poles. Conducting (graphite) and dielectric alumina (Al_2O_3) covers were manufactured and tested with the thruster. The conducting graphite cover was evaluated due to its low sputter yield, whereas the dielectric alumina cover was evaluated because it provides a configuration that is similar to flight thrusters. Figure 1 shows photographs of TDU-1 with the graphite and alumina front pole covers.

After incorporating the design changes into the TDU-1 thruster, the 2016 test campaign was initiated. The key tests planned for this test campaign included:

1. Evaluation of TDU-1 performance and stability at selected firing conditions. Performance was evaluated for a range of thruster magnetic field strengths and for the two thruster front cover pole configurations (conducting and dielectric);

2. Evaluation of the TDU-1 performance and stability at the selected firing conditions for three candidate thruster body electrical configurations that included: grounded (GND), floating (F), and cathode-to-thruster tied (C-T) configurations. The main objective of the TDU-1 electrical configuration tests was to determine the most representative ground test configuration relative to in-space operation. An accompanying paper by Peterson presents detailed results from the various electrical configuration tests;[15]

3. Characterization of the thruster operation and stability under various facility background pressure conditions;

Figure 1. The HERMeS TDU-1 Hall thruster with dielectric (left) and conducting (right) front pole covers.

4. Characterization of TDU-1 thermal performance. This included steady-state temperature measurements of critical thruster components. An accompanying paper by Myers reports on the results of the thermal characterization tests and thermal modeling of the thruster;[16]

5. Characterization of the front pole cover erosion for the two candidate pole cover materials: graphite and alumina. This entailed performing two short duration wear tests to measure the inner and outer front pole cover erosion for both materials. An accompanying paper by Williams reports on the results of the short duration wear tests;[17]

6. Characterization of the TDU-1 plume at the selected thruster firing conditions. For these measurements a Faraday probe (FP), Wien filter spectrometer (WFS or $\mathbf{E} \times \mathbf{B}$), retarding potential analyzer (RPA), and Langmuir probe (LP) were employed. Results from these measurements are included in an accompanying paper;[18]

7. Characterization of the facility back sputter rate during thruster tests. An accompanying paper by Gilland reports on the impact of the back sputter rate on the thruster operation and thruster wear prediction;[19] and
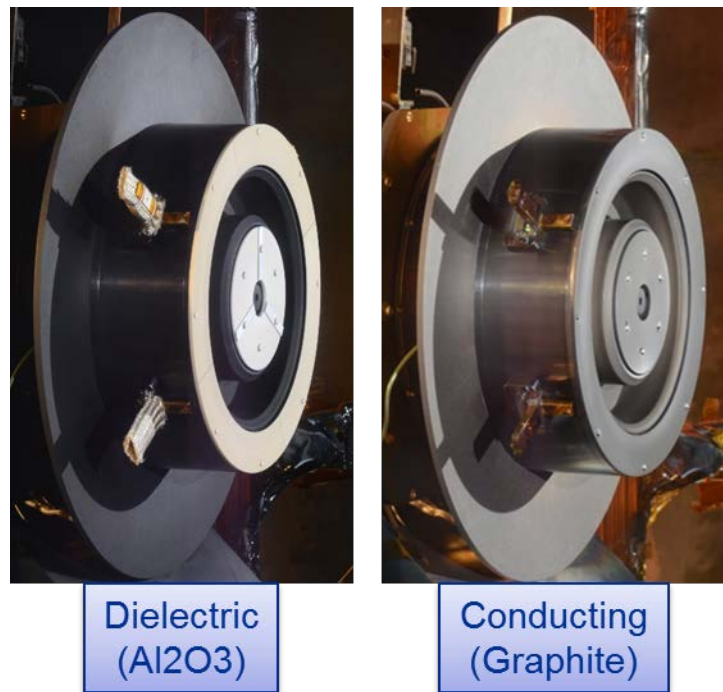
8. Performing an extended duration test of TDU-1 after completion of tests 1-7 (listed above). The objective of the test is to confirm that front pole erosion has been mitigated and to uncover any unknown issues that may inhibit the thruster from meeting its performance and propellant throughput specifications.

Results from the performance, stability, and pressure effects characterization of the TDU-1 thruster at selected thruster firing conditions are presented herein. Section III summarizes the experimental setup and the test hardware; Section IV presents the thruster performance at the selected thruster firing conditions, Section V presents the results of the facility background pressure effects characterization tests, Section VI presents the results of the stability assessment at the selected firing conditions and at the various operating elevated pressure conditions; and Section VI presents a summary and conclusion of the present work.

III. Experimental Apparatus

A. Hall Effect Rocket with Magnetic Shielding TDU-1

The 12.5 kW HERMeS TDU-1 was installed inside Vacuum Facility (VF-5) at NASA GRC. The design of HERMeS incorporates technologies developed by NASA over nearly two decades. The thruster incorporates a magnetic shielding topology to eliminate discharge channel erosion as a life limiting mechanism.[3,20,21,22,23] The result is a significant increase in the operational lifetime, with HERMeS being designed to operate at 3000 s specific impulse with a lifetime exceeding 50,000 hours.

The HERMeS TDU-1 Hall thruster was fabricated at NASA GRC. The first test campaign was completed in 2015.

The test apparatus enabled the TDU-1 thruster to be operated in three different electrical configurations (GND, F, and C-T). Changing between each of the electrical configurations was performed outside the chamber within the thruster break-out-box (BOB).

B. Vacuum Facility

Testing of the HERMeS TDU-1 thruster was performed in VF-5 at NASA GRC. Figure 2 shows the VF-5 graphite lined chamber walls. Full details on the facility can be found in Ref. [24] The main chamber is 4.6 m in diameter, 18.3 m long, and can be evacuated with cryopanels and/or oil diffusion pumps. For the test campaign discussed in this paper, the TDU-1 Hall thruster was located in the main volume of the chamber to ensure the lowest possible background pressure during thruster operation.[25] Facility pressure was monitored with three xenon and one air calibrated (#2) ion gauges (IGs) during thruster operation. The location and orientation of the four IGs are shown in Fig. 3. Ion gauge 3 was employed as the main pressure reading during operation based on the modeling results and experimental experience indicating that it provides the most representative reading of the facility background pressure.[3,25]
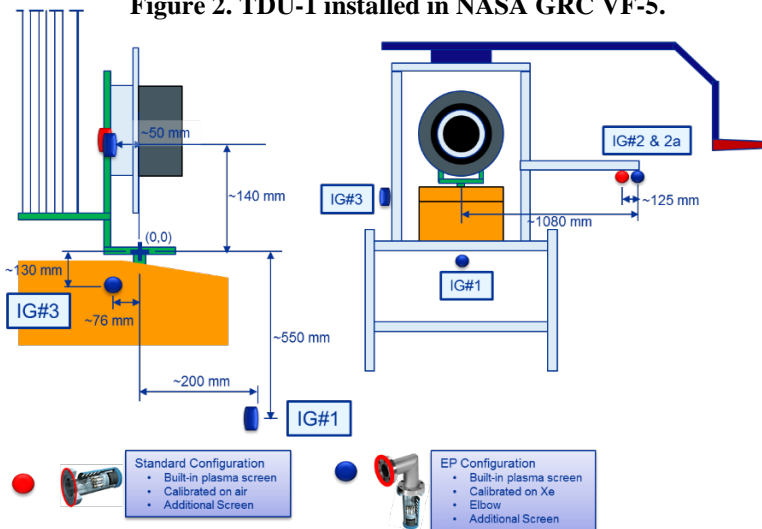

Figure 2. TDU-1 installed in NASA GRC VF-5.

Figure 3. Schematic of the internal ion gauge setup for the TDU-1 test campaign, sketch not to scale.

C. Power Supplies, Data Acquisition, and Control Systems

For the HERMeS TDU-1 test campaign the thruster was powered with a laboratory power rack that contained the discharge, inner and outer electromagnet, cathode heater, and cathode keeper power supplies. The discharge power supply consists of three 15 kW (1000 V and 15 A) power supplies that were connected in a master-slave configuration. A computer was used to sweep the thruster discharge voltage during the thruster IVB (current-voltage-magnetic) stability characterization test.

The data acquisition system used for the TDU-1 tests was a multiplexed datalogger with computer interface. The datalogger monitored the voltages, currents, temperatures, propellant flow rates, chamber pressure, and thrust at 1 Hz during performance testing. The computer interface had the additional benefit of allowing a number of channels to be monitored with failsafe limits for unattended operation. The uncertainties of the datalogger measurements were ±0.05% for the voltage and current measurements.

D. Flow System

A laboratory propellant feed system was used in the TDU-1 test campaign. The feed system supplied xenon to the thruster and was also used to elevate the facility background pressure. The propellant feed system utilized four mass flow controllers (MFC). A 500 and a 100 sccm MFC supplied xenon propellant to the thruster and cathode, respectively. A 200 and 1,000 sccm MFC supplied xenon to elevate the chamber pressure, its auxiliary flow was injected at mid chamber and was directed toward the chamber end cap opposite to thruster location. The MFC calibration curves indicated that the anode and cathode flow rate uncertainties are ≤1% of the set value.

E. Diagnostics
1. Thrust Stand

The performance of the TDU-1 Hall thruster was measured with an inverted pendulum null-type thrust stand. The NASA GRC high-power thrust stand has an accuracy of ≤1% based on a statistical analysis of the calibration and thrust zero data taken throughout the test campaign. The operation and theory of the inverted pendulum null-type thrust stand are described in detail in Refs. 26 and 27. The high-power thrust stand was operated in a null-type configuration, which allows the thruster to remain stationary while testing. The thrust stand was also equipped with a closed loop inclination control circuit, which utilized a piezoelectric element to minimize thermal drift during thruster tests. The thrust stand was calibrated in-situ with known masses on a pulley system connected to a stepper motor. The thrust stand was calibrated before and after each performance mapping period.

2. Plasma Plume

A variety of plasma diagnostics were simultaneously deployed during thruster tests. These diagnostics include far-field Faraday probe, retarding potential analyzer, accompanying Langmuir probe, WFS probe, and infrared (IR) camera system. Figure 4 shows a photograph of the probe array used in VF-5. The plasma plume diagnostics are described in detail in Ref. 18. The probe array was mounted on a two-axis polar positioning system (shown in Fig. 3). Data collected included ion current density, ion energy per charge, and species composition as functions of polar angle and distance from the thruster. These data will be used for spacecraft interaction, thruster performance, and facility effect studies. Results of the spacecraft interaction studies will provide guidelines for the design of vehicles that may use HERMeS, including the Asteroid Redirect Robotic Mission vehicle. The thruster performance studies will be

Figure 4. The plasma plume probe array used for the TDU-1 test campaign.

used to characterize and form a baseline for various aspects of the thruster that can affect its performance and life. The results of both studies will also be projected to a space-like environment in order to predict on-orbit thruster and plume characteristics as well as differences from ground-test characteristics.
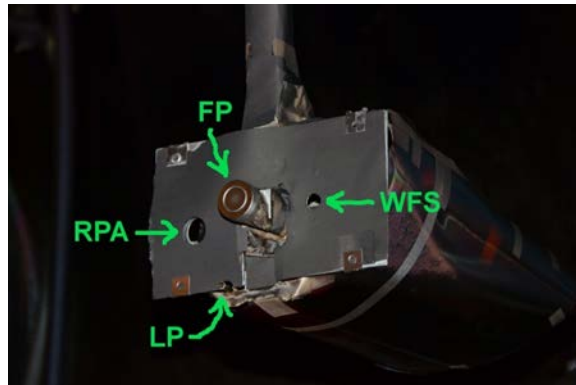
3. Time Resolved Thruster Telemetry

The temporal behavior of the TDU-1 Hall thruster key parameters were continuously monitored by multiple oscilloscopes. The oscilloscope telemetry included both AC and DC monitoring of the thruster discharge current and voltage, thruster body voltage and current, cathode-to-ground voltage, and other key cathode parameters. The internal

functionality of the oscilloscopes was used to calculate the root mean square (RMS), peak-to-peak (Pk2Pk), and mean value where appropriate. The oscilloscope telemetry was recorded using the data acquisition system on the same time scale as the other telemetry. The logging of the thruster temporal characteristics provided additional information on the high-speed IVB sweep that was useful when analyzing the thruster stability. Additionally a dedicated oscilloscope was used to record five million points of data on the discharge current and voltage for generation of power speectral density (PSD) plots at selected thruster operating conditions.

IV. TDU-1 Performance Evaluation Results

A. Performance

The TDU-1 thruster performance was evaluated for the graphite and alumina (Al_2O_3) front pole cover configurations. Thruster performance was evaluated at power levels between 1.8 and 12.5 kW. The thruster magnetic field strength was varied across the operational range to assess the variation of thruster performance with magnetic field. The cathode flow rate was set to 7% of the anode flow. For all data presented in this paper, the magnetic field was normalized to an arbitrary value. The sections below present the results from the TDU-1 performance tests for the graphite and alumina front pole cover configurations.

1. Graphite Front Pole Cover Configuration

For the TDU-1 thruster with graphite pole cover configuration, the thruster body tied to cathode (C-T) electrical configuration was selected. This configuration, as is detailed in Ref. 15, provides a viable thruster configuration that can provide the performance and propellant throughput capability to meet the ARRM mission needs. The configuration is viable due to the low sputter yield of graphite and the low DC and AC thruster body voltages with respect to ground when the thruster body is electrically connected to the cathode. Operating TDU-1 in a floating electrical configuration caused the thruster body to have large negative DC potentials along with very large negative Pk2Pk oscillations on the thruster body voltage. The large negative DC and AC thruster body potential would result in high thruster front pole cover erosion rates that will greatly reduce the throughput capability of the thruster.

For this test campaign, the thruster performance was evaluated for discharge power levels between 1.8 and 12.5 kW. Figure 5 shows a photograph of the thruster during operation at full power. Table 1 lists the thruster operating conditions where the performance evaluation was conducted.

Table 1. TDU-1 thruster operating conditions with the graphite front pole cover.

Thruster Discharge Voltage, V	300	300	400	500	500	600	700
Thruster Discharge Current, A	6	20.8	20.8	20.8	25	20.8	17.8
Thruster Discharge Power, kW	1.8	6.3	8.3	10.4	12.5	12.5	12.5

Figure 6 presents the TDU-1 thrust variation with applied magnetic field. The trends in Fig. 6 indicate that the variation in thrust is within 5% across the range of all magnetic fields that were tested. In general, the thrust tended to slightly increase with increased magnetic field except for the 300 V discharge voltage operation where thrust decreased with increased magnetic field strength. Figure 7 presents the total mass flow rate variation with applied magnetic field. Results in Fig. 7 indicate that the total mass flow rate decreased with increased magnetic field strength. Results in Fig. 7 also show that at 20.8 A discharge current operation, increased discharge voltage operation required increased anode flow to maintain the discharge current at a given level.
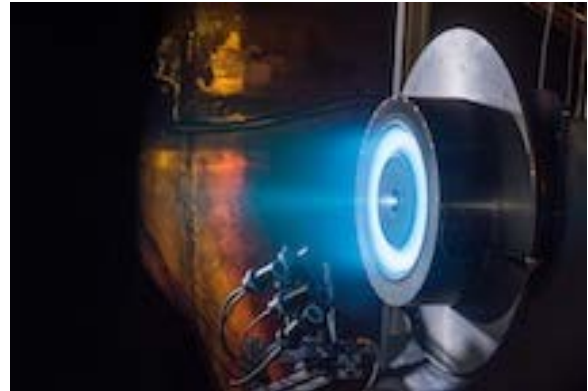

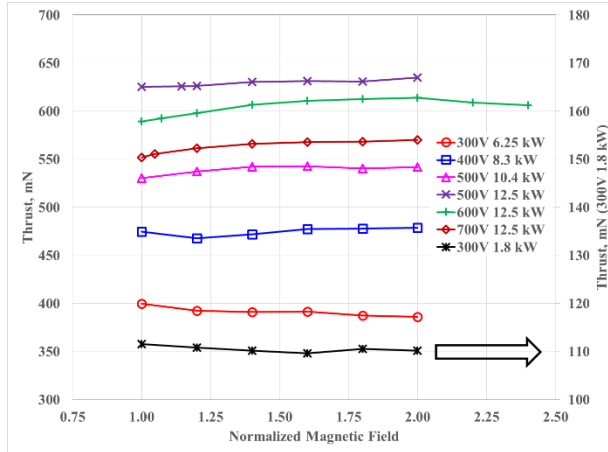**Figure 5. TDU-1 thruster operating in NASA GRC's VF-5.**

Figure 6. TDU-1 thrust variation with normalized magnetic field at the selected operating conditions for the graphite front pole cover configuration.
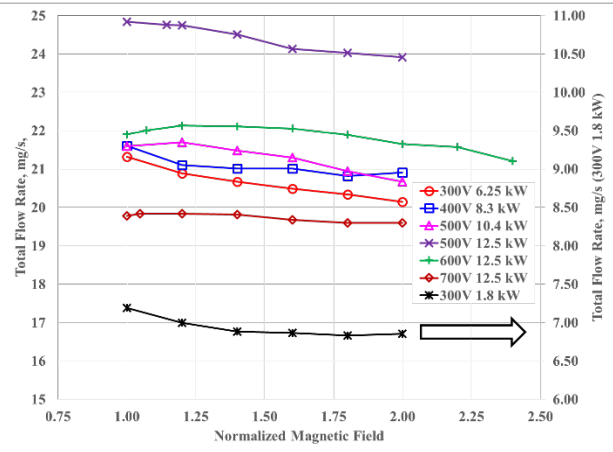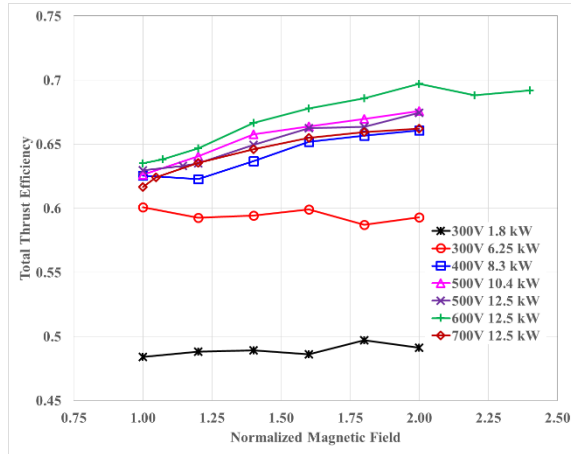

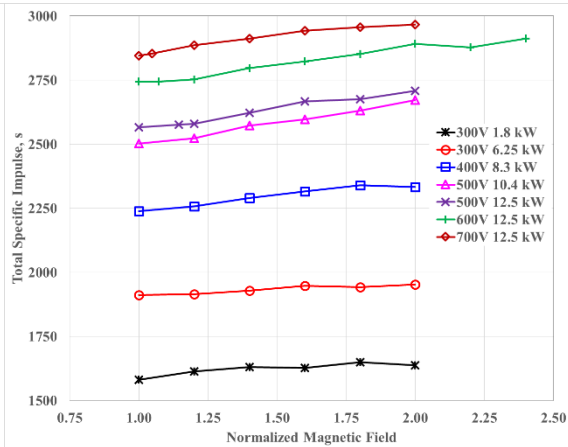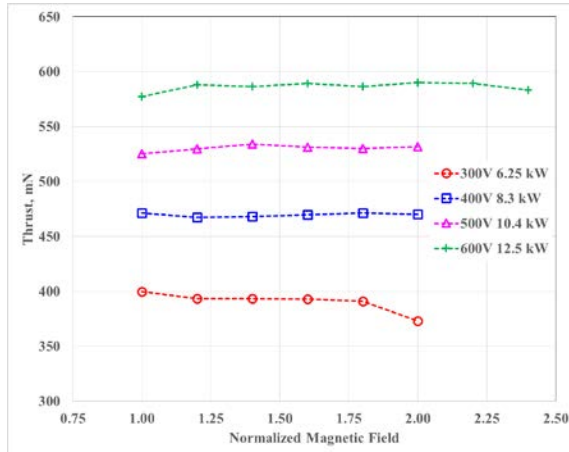**Figure 7. TDU-1 total mass flow rate variation with normalized magnetic field at the selected operating conditions for the graphite front pole cover configuration.**

Figures 8 and 9 present the total thrust efficiency and total specific impulse variation with magnetic field for the TDU-1 thruster. Results in Fig. 8 indicate that at 300 V operation, thrust efficiencies of approximately 49% and 60% were achieved at 1.8 and 6.25 kW, respectively, and the magnitude was mostly unchanged with increased magnetic field. At higher discharge voltages, thrust efficiencies increased with increased magnetic field. At a normalized field strength of 1.6, thrust efficiencies of approximately 65% were attained at discharge voltages of 400, 500, and 700 V. At a discharge voltage of 600 V a thrust efficiency of 68% was attained. Increases in the normalized magnetic field beyond 1.6 resulted in additional improvements to the thruster efficiency. Results in Fig. 9 show a similar trend. At a normalized field strength of 1.6, a specific impulse of 1,950 s, 2,320 s, 2,600 s, 2,670 s, 2,823 s, and 2,940 s was demonstrated at 300V/6.25kW, 400V/8.3kW, 500V/10.4kW, 500V/12.5kW, 600V/12.5 kW, and 700V/12.5kW, respectively. The combination of increased thrust and lower mass flow rates with increased magnetic field, at a given discharge voltage operating point, resulted in the total thrust efficiency and total specific impulse increasing with magnetic field.

Figure 8. TDU-1 total thrust efficiency variation with normalized magnetic field at the selected operating conditions for the graphite front pole cover configuration.

Figure 9. TDU-1 total specific impulse variation with normalized magnetic field at the selected operating conditions for the graphite front pole cover configuration.

2. Alumina Front Pole Cover Configuration

For the testing conducted with the alumina pole covers, an electrical configuration where the thruster body was floating relative to facility ground was selected. This configuration, as is detailed in Ref. 15, provides a thruster configuration that is similar to flight thruster operation. For this test series, the thruster performance was evaluated at power levels between 6.25 and 12.5 kW as shown in Table 2.

Table 2. TDU-1 thruster operating conditions with the Al$_2$O$_3$ front pole cover.

Thruster Discharge Voltage, V	300	400	500	600
Thruster Discharge Current, A	20.8	20.8	20.8	20.8
Thruster Discharge Power, kW	6.25	8.33	10.4	12.5

Figures 10 and 11 present the TDU-1 thrust and total mass flow variation with magnetic field for the alumina front pole cover configuration. Results in Fig. 10 indicate that the thrust was almost invariant to changes in the thruster's magnetic field. Results in Fig. 11 show that at a given discharge voltage, the thruster mass flow rate decreased with increasing magnetic field and that increasing the discharge voltage required an accompanying increase in the anode flow rate to maintain the discharge current at 20.8 A.

Figures 12 and 13 present the TDU-1 total thrust efficiency and total specific impulse variations with magnetic field. In general, the total thrust efficiency and total specific impulse increased with increased magnetic field. These increases were associated with the fact that although the thrust did not increase with magnetic field, the thruster's mass flow rate decreased indicating improved ionization and increased mass utilization. Results in Fig. 12 indicate that at 300 V operation, thrust efficiencies of approximately 60% were achieved at 6.25 kW, and the magnitude was mostly unchanged with increased magnetic field (except at a normalized field strength of 2). At higher discharge voltages, thrust efficiencies increased with increased magnetic field. The normalized magnetic field strength of 1.6 was selected as the nominal operating point for the various thruster operating conditions. At a normalized magnetic field strength of 1.6, thrust efficiencies of approximately 64% were attained at discharge voltages of 400, 500, and 600 V. Increases in the normalized magnetic field beyond 1.6 resulted in additional improvements to the thruster efficiency. Results in Fig. 13 show a similar trend for total specific impulse. At a normalized field strength of 1.6 a specific impulse of 1,960 s, 2,300 s, 2,560 s, and 2,800 s were demonstrated at 300V/6.25kW, 400V/8.3kW, 500V/10.4kW, and 600V/12.5kW, respectively. The constant thrust and lower mass flow rates with increased magnetic field resulted in the total thrust efficiency and total specific impulse increasing with magnetic field.

Figure 10. TDU-1 thrust variation with normalized magnetic field at selected operating conditions for the alumina front pole cover configuration.
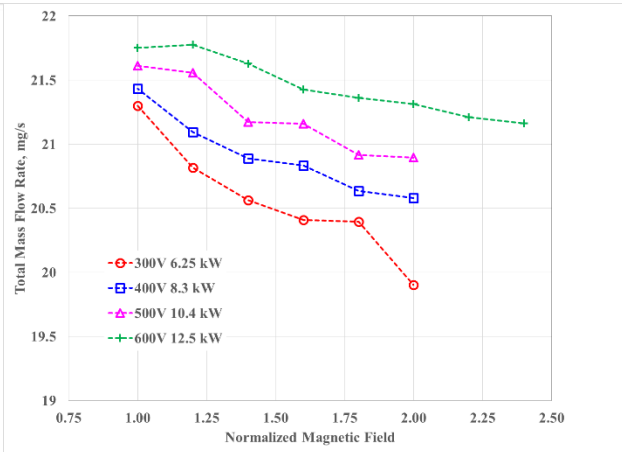
Figure 11. TDU-1 total mass flow rate variation with normalized magnetic field at selected operating conditions for the alumina front pole

3. Comparison of Graphite and Alumina Thruster Performance

Figures 14-17 compare the thrust, total mass flow rate, total thrust efficiency, and total specific impulse results between the graphite and alumina pole cover configurations for thruster operation at discharge voltages of 300-600 V and a discharge current of 20.8 A. As is shown in Figs. 14 and 15, at 300 V, the thrust and mass flow rates for the two configurations are similar. At discharge voltages of 400 V and higher, the graphite C-T configuration has higher thrust and higher mass flow rate at a given magnetic field than the alumina F configuration. Figures 16 and 17 indicate that
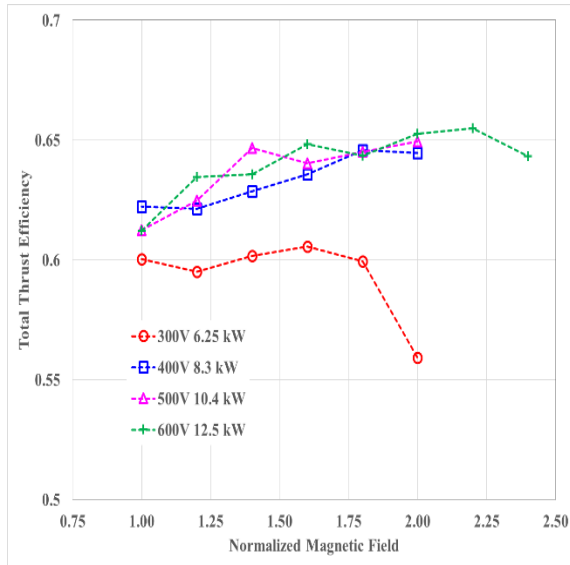
Figure 12. TDU-1 total thrust efficiency variation with normalized magnetic field at selected operating conditions for the alumina front pole cover configuration.
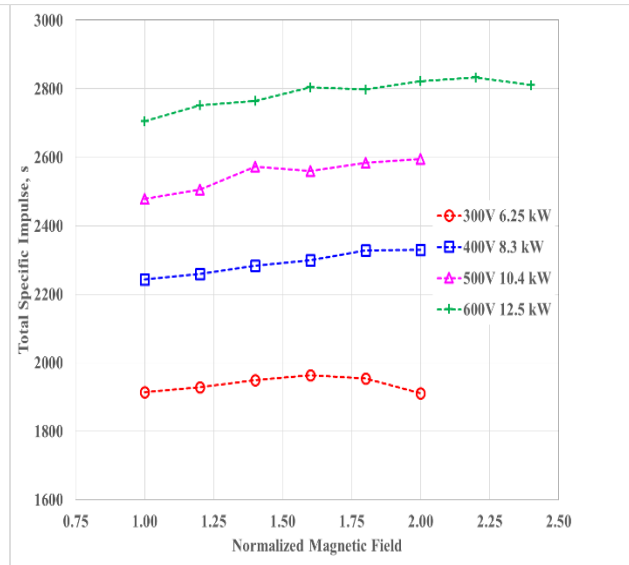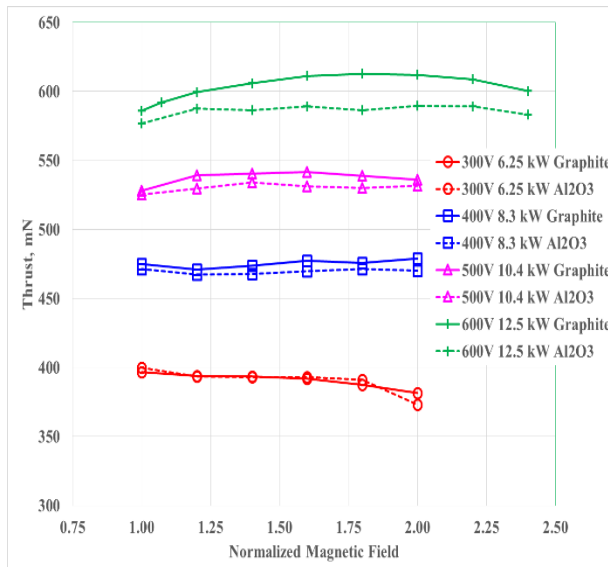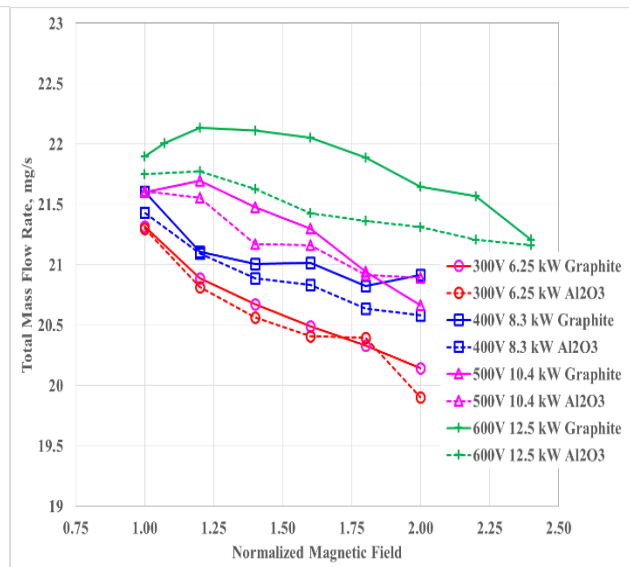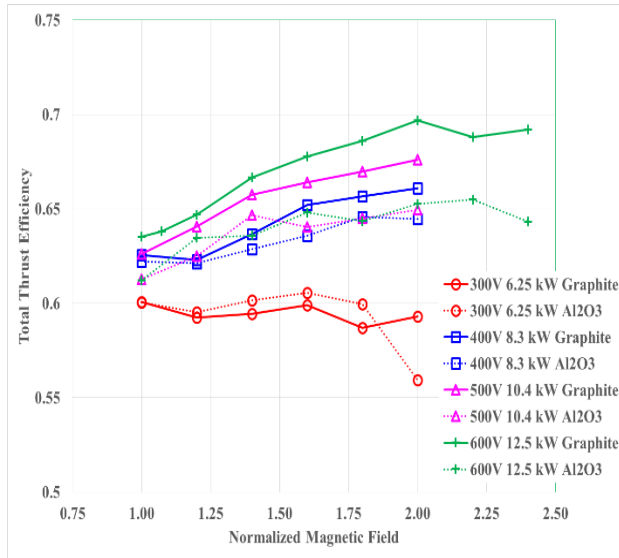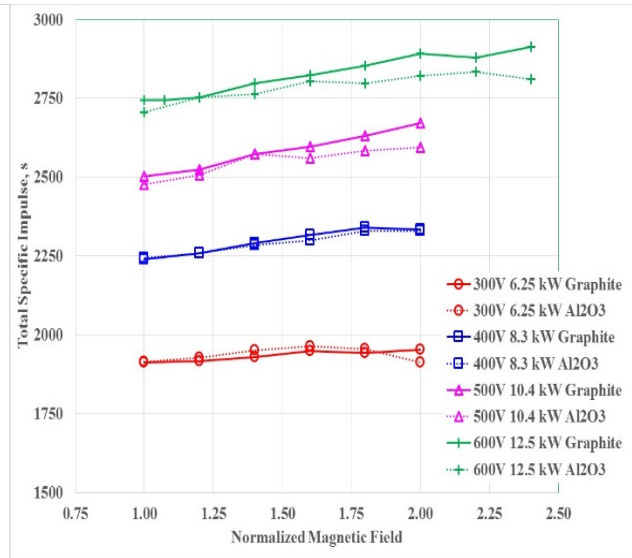
Figure 13. TDU-1 total specific impulse variation with normalized magnetic field at selected operating conditions for the alumina front pole cover configuration.

the graphite C-T configuration has a higher thrust efficiency than the alumina F configuration; this is attributed to the higher thrust magnitudes that were realized for the graphite C-T configuration. Results in Fig. 17 show that the total specific impulse magnitudes for the two configurations are very similar because the higher thrust demonstrated during graphite C-T operation required higher mass flow rates to maintain the thruster's discharge current. The differences in thruster performance between the two configurations are not only attributed to the change in the pole cover material (i.e., from conducting graphite to dielectric alumina) but can also be attributed to the different electrical configuration of the thruster (C-T vs F).[15]

Figure 14. TDU-1 thrust variation with normalized magnetic field at selected operating conditions for graphite and alumina front pole cover configurations.

Figure 15. TDU-1 total mass flow rate variation with normalized magnetic field at selected operating conditions for graphite and alumina front pole cover configurations.

9
American Institute of Aeronautics and Astronautics

Figure 16. TDU-1 total thrust efficiency variation with normalized magnetic field at selected operating conditions for graphite and alumina front pole cover configurations.

Figure 17. TDU-1 total specific impulse variation with normalized magnetic field at selected thruster operating conditions for graphite and alumina front pole cover configurations.

B. TDU-1 Discharge Current and Voltage Oscillations

To characterize the TDU-1 thruster stability, high speed measurements of discharge current oscillations were performed. The discharge current Pk2Pk and RMS were used to provide an assessment of the thruster stability.[28,29] Figure 18 presents the graphite C-T normalized discharge current Pk2Pk and RMS plots for the selected thruster operating points with varying magnetic field. As is shown in Fig. 18, the thruster's discharge oscillations grow in magnitude with increased discharge voltage. For 300V/1.8kW operation, the discharge is very quiescent; the oscillation's magnitude grows as the thruster is transitioned to higher discharge current operation of 20.8 A. At a discharge voltage of 400 V, the thruster is still operating in a very quiescent mode as is evident from the normalized Pk2Pk and RMS profiles. At 500V/10.4kW, the thruster's mode changes and mode transition to a higher oscillatory mode occurs as will be shown later. At 500V/10.4kW, the normalized Pk2Pk and RMS reach values of 95% and 0.18, respectively, which were among the highest recorded. At 500V/12.5kW, the thruster oscillations are still characterized by large normalized Pk2Pk values of approximately 80-90%. At 600V/12.5kW, the normalized discharge current Pk2Pk and RMS are still exhibiting large oscillations, and that trend continues to thruster operation at 700V/12.5kW. The results in Fig.18 clearly show that at discharge voltages of 500 V and above, the thruster transitioned to a higher oscillatory mode. Results in Fig. 18 also showed that the magnetic field did impact the level of oscillations, and this was more pronounced at discharge voltage operation above 400 V.

Figure 19 presents the normalized discharge current Pk2Pk and RMS variations with magnetic field for the alumina F thruster configuration. The results in Fig. 19 show similar trends as Fig. 18; at discharge voltages of 300 and 400 V, the thruster is operating in a quiescent mode that is characterized by small oscillation magnitudes. At discharge voltages of 500 and 600 V, the thruster oscillation magnitude grows and the thruster transitions to a more oscillatory mode. Comparison of results from Figs. 18 and 19 indicates that the thruster operation in the graphite C-T configuration resulted in a more oscillatory thruster behavior when compared to the alumina F configuration. This higher oscillatory behavior did not result in any reduction in thruster performance as was shown in Figs. 16 and 17.
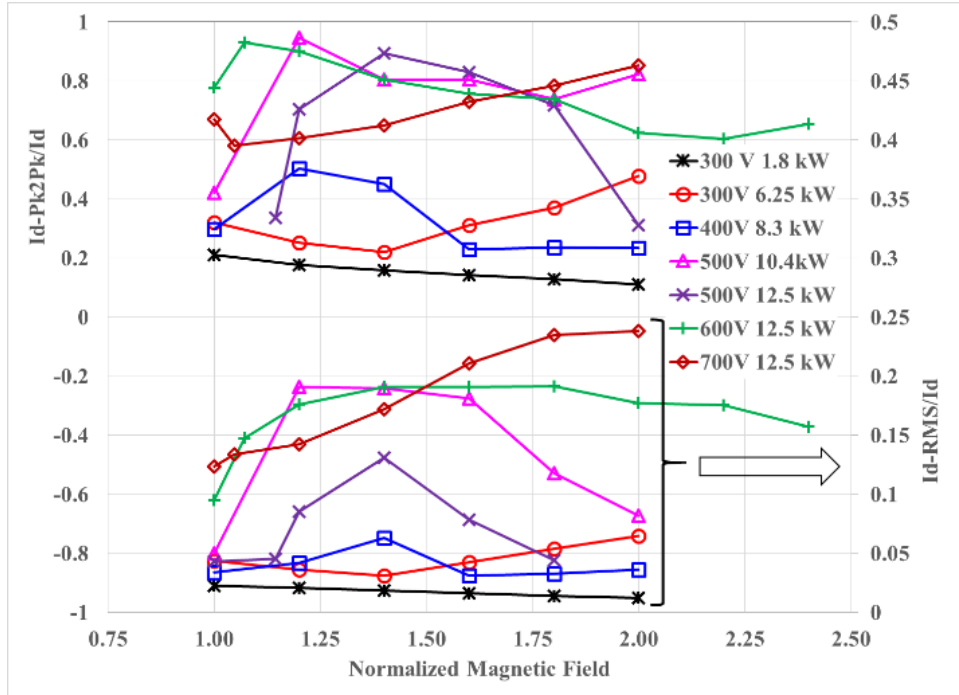
Figure 18. TDU-1 normalized discharge current Pk2Pk and RMS variation with normalized magnetic field at selected operating conditions for graphite C-T front pole cover configuration.
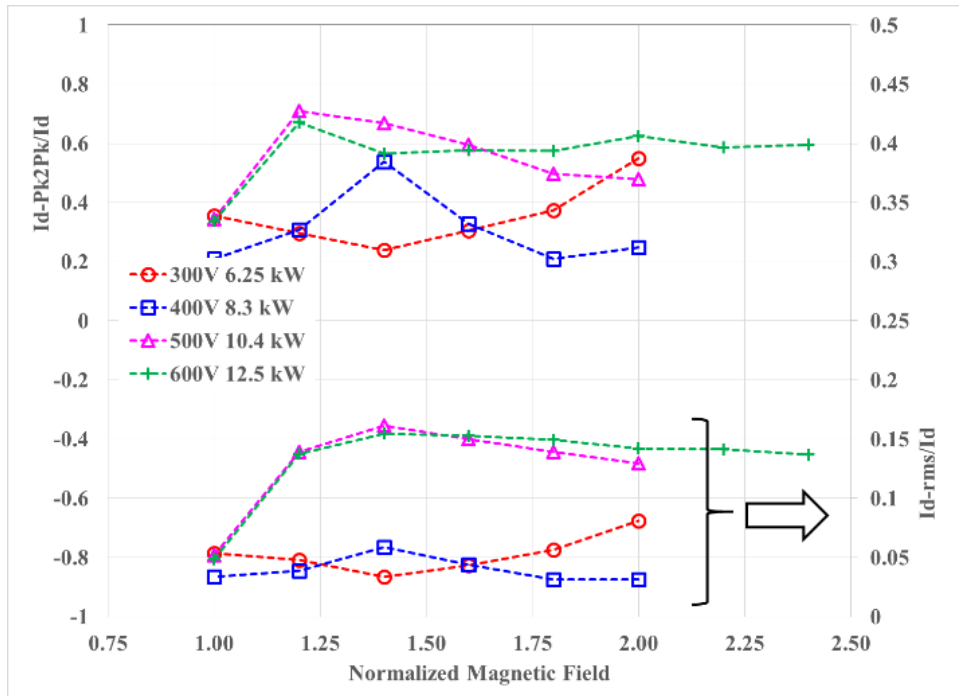

Figure 19. TDU-1 normalized discharge current Pk2Pk and RMS variation with normalized magnetic field at selected operating conditions for the alumina front pole cover configuration.

C. Current-Voltage-Magnetic Field Maps

Detailed IVB sweeps were performed for the graphite C-T configuration. The IVB sweeps were performed by setting the anode and cathode flow rate (typically to 7% of anode flow rate), setting the thruster's magnetic field strengths, and then ramping the discharge voltage at increments of 5 V every 2 sec for a selected voltage range. The IVB sweeps were performed at anode flow rates between 6.4 and 22.5 mg/s. The normalized magnetic field strength was varied between 0.6 and 2 (except for 20.5 mg/s operation where it varied between 0.6 and 2.4).

1. Graphite Pole Cover Cathode Tied to Thruster Configuration

Table 3 lists the IVB sweep anode flow rates, voltage sweep range, electrical configuration, and pressure levels. In this section, the results at the lowest facility background pressure will be presented for the graphite C-T configuration. The IVB sweeps at the elevated VF-5 background pressures (i.e, mid and high pressure) will be presented in a later section.

Table 3. TDU-1 IVB sweeps test conditions for the graphite C-T configuration. (LP: Lowest Pressure, MP: Mid Pressure, HP: High Pressure, C-T: Cathode tied to thruster, F: Floating, and GND: Thruster Body Grounded).

Anode Flow Rate, mg/s	Voltage Sweep Range, V	Electrical Configuration	Pressure
6.4	200-400	C-T, F, GND	LP, MP, HP
9.8	200-400	C-T, F, GND	LP, MP, HP
15.3	200-400	C-T, F, GND	LP, MP, HP
18.4	300-710	C-T, F, GND	LP, MP, HP
19.3	300-650	C-T, F, GND	LP, MP, HP
20.5	200-650	C-T, F, GND	LP, MP, HP
21.0	400-600	C-T	LP
21.5	400-600	C-T	LP
22.0	400-600	C-T	LP
22.5	300-510	C-T, F, GND	LP, MP, HP

The IVBs at 19.3, 21, 21.5 and 22 mg/s will not be presented in this paper since results at 18.4 and 20.5 mg/s are representative of the trends found at 19.3, 21, 21.5 and 22 mg/s. Results in Figs. 20-25 present 3D contour plots of the normalized discharge current RMS as a function of the discharge voltage (x axis), normalized magnetic field (y axis), and discharge current (z axis).

Figure 20 presents the IVB sweep results at 6.4 mg/s. The results indicate an average normalized RMS discharge current value of ~0.1 across the various magnetic field settings (except at discharge voltages of 300-400 V at the lowest magnetic field setting) which indicates quiescent and stable thruster operation. Figure 21 presents similar trends for a thruster flow rate of 9.8 mg/s, where the discharge current oscillation magnitudes increase at discharge voltages between 300-400 V at the lowest magnetic field operating setting. In addition, Fig. 21 indicates that the region of increased oscillations is growing as the thruster flow rate was increased from 6.4 to 9.8 mg/s.
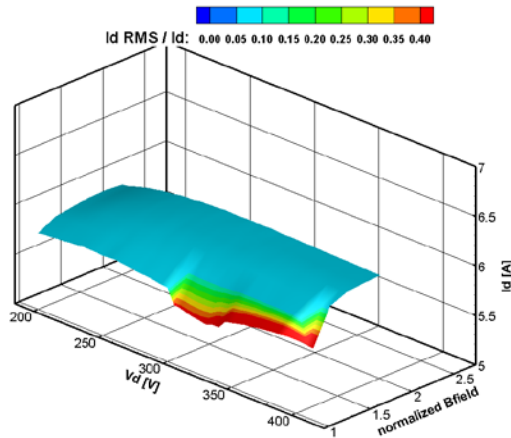
Figure 20. IVB map of normalized Id-RMS at 6.4 mg/s for the graphite cover C-T thruster configuration at a background pressure of 1.8 µTorr-Xe.
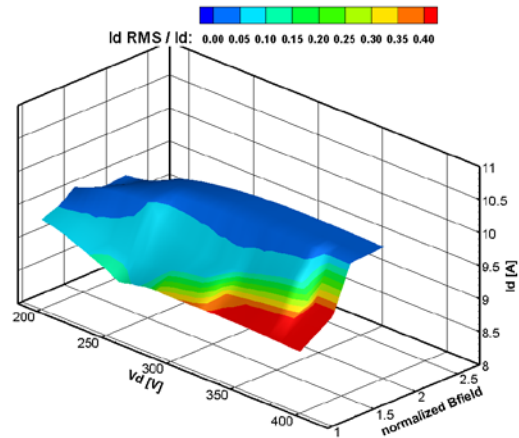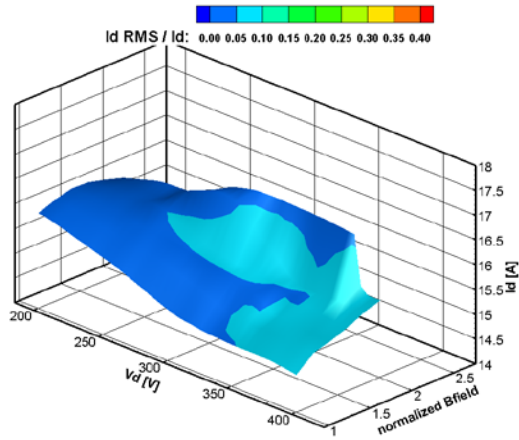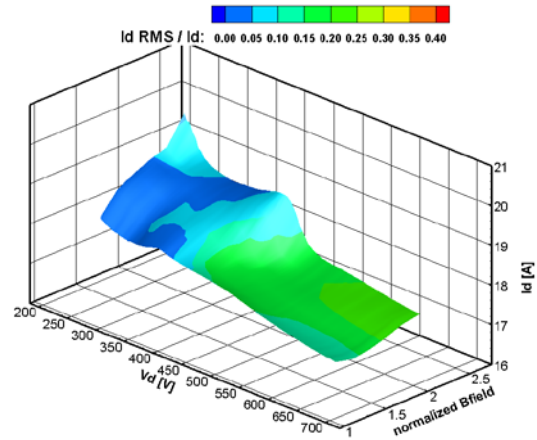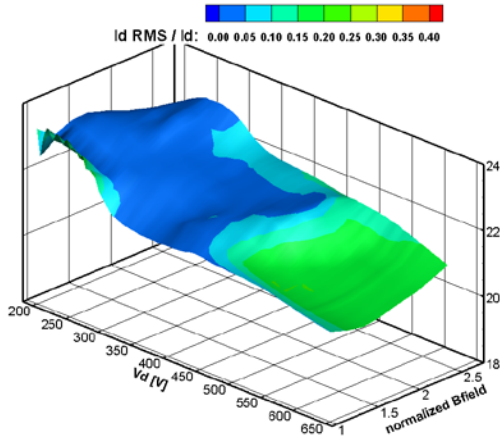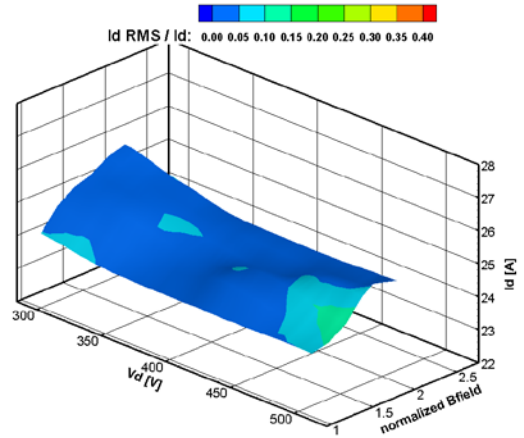

Figure 21. IVB map of normalized Id-RMS at 9.8 mg/s for the graphite cover C-T thruster configuration at a background pressure of 2.7 µTorr-Xe.

Figure 22 presents the IVB sweep results at 15.3 mg/s and indicates lower discharge oscillation magnitudes when compared to 6.4 and 9.8 mg/s operation. Figure 23 presents the IVB sweep results at 18.4 mg/s with a discharge voltage sweep range from 300 to 710 V. Results in Fig. 23 show that the normalized RMS magnitude increases for voltages above 400 V (seen earlier from Figs. 18 and 19). The increased magnitudes (~0.2-0.3) indicate that the thruster transitioned to another mode but the magnitudes of the normalized RMS are still consistent with thruster operation in steady state while having high performance and no thermal issues.

Figure 24 presents the IVBs at 20.5 mg/s. Results in Fig. 24 indicate stable thruster operation for the entire voltage sweep range (Id-RMS/Id < 0.3), but the IVB sweep clearly shows where the thruster transitioned modes at a discharge voltage slightly above 400 V. This again matches the results presented in Fig. 17. Finally, Fig. 25 presents the IVB sweep results at 22.5 mg/s. Results in Fig. 25 indicate that at discharge voltages below ~400 V the thruster operation was very quiescent and that it started transitioning to a more oscillatory operation above 400 V, which is similar to what was found for the 15.3, 18.4, and 20.5 mg/s IVB sweeps.
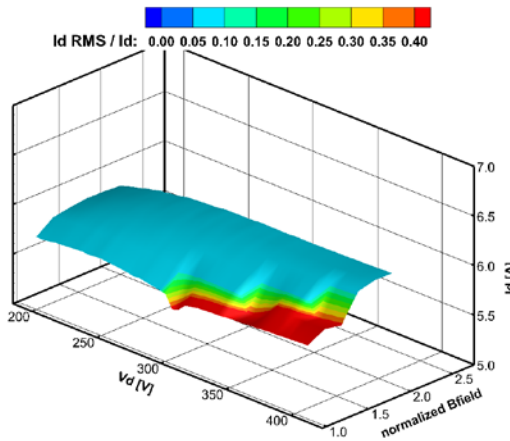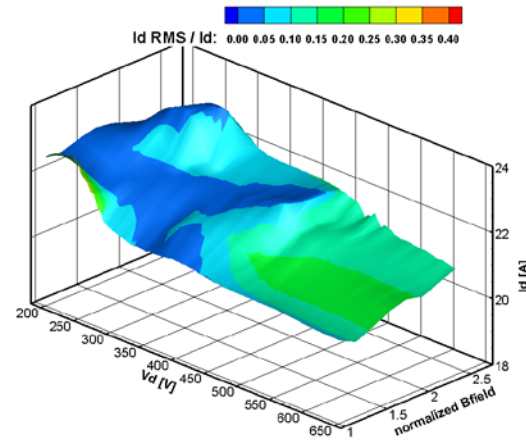

Figure 22. IVB map of normalized Id-RMS at 15.3 mg/s for the graphite cover C-T thruster configuration at a background pressure of 4 µTorr-Xe.

Figure 23. IVB map of normalized Id-RMS at 18.4 mg/s for the graphite cover C-T thruster configuration at a background pressure of 4.1 µTorr-Xe.

Figure 24. IVB map of normalized Id-RMS at 20.5 mg/s for the graphite cover C-T thruster configuration at a background pressure of 5.1 µTorr-Xe.
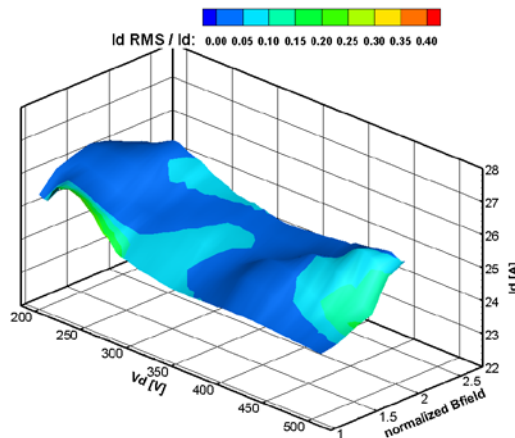

Figure 25. IVB map of normalized Id-RMS at 22.5 mg/s for the graphite cover C-T thruster configuration at a background pressure of 5.05 µTorr-Xe.

2. Alumina Pole Cover Floating Configuration

Abbreviated IVB sweeps were performed for the alumina F configuration. The IVB sweeps were performed at anode flow rates of 6.4, 20.2, and 22.5 mg/s. Only an abbreviated set was acquired to compare with the results of the graphite C-T configuration. Table 4 lists the IVB sweep anode flow rates, voltage sweep range, electrical configuration, and pressure levels. In this section, the results at the lowest facility background pressure will be presented for the alumina F configuration.

Table 4. TDU-1 IVB sweeps test conditions for the alumina F thruster configuration.

Flow Rate, mg/s	Voltage Sweep Range, V	Electrical Configuration	Pressure
6.4	200-400	C-T, F, GND	LP
20.2	200-650	C-T, F, GND	LP, MP, HP
22.5	300-510	C-T, F, GND	LP

Figure 26 presents the IVB sweeps at 6.4 mg/s. The results look very similar to the results presented in Fig. 20 for the graphite C-T configuration. Figure 27 presents the IVB sweeps at 20.2 mg/s. These results indicate a qualitatively similar behavior to the results in Fig. 24 (for the graphite C-T) with slightly lower normalized RMS magnitudes for the alumina F thruster configuration, which matches findings from Figs. 18 and 19 at 500 and 600 V thruster operation. Finally, Fig. 28 presents the IVB sweeps at 22.5 mg/s. The results in Fig. 28 are qualitatively similar to results in Fig. 25, but the alumina F configuration is indicating slightly higher normalized RMS magnitudes at discharge voltages above 400 V.

Figure 26. IVB map of normalized Id-RMS at 6.4 mg/s for the alumina cover F thruster configuration at a background pressure of 1.8 µTorr-Xe.

Figure 27. IVB map of normalized Id-RMS at 20.2 mg/s for the alumina cover F thruster configuration at a background pressure of 4.45 µTorr-Xe.

Figure 28. IVB map of normalized Id-RMS at 22.5 mg/s for the alumina cover F thruster configuration at a background pressure of 4.92 µTorr-Xe.

D. Power Spectral Density Analysis of Discharge Current Waveforms

Power spectral density (PSD) analysis was performed on the discharge current waveforms during thruster operation at varying magnetic field strength. The discharge current waveforms for the graphite C-T and alumina F configurations were analyzed to determine the thruster's dominant breathing mode frequency and to further elucidate the mode transitions during thruster operation. For the graphite C-T and alumina configurations, results will be presented for thruster operation at 300V/6.25kW, 400V/8.3 kW, 500V/10.4 kW, and 600V/12.5kW.

1. Graphite Front Pole Cover Cathode Tied Thruster Configuration

Figure 29 presents the PSDs for thruster operation at 300V/6.25 kW. These profiles indicate that at lower magnetic field strength, the dominant frequency is ~10 kHz with a strong secondary frequency at ~70 kHz. Increasing the magnetic field above the normalized field strength of 1.2 results in the dominant frequency shifting to lower frequencies, as is shown in Fig. 29, and the secondary oscillation energy being dramatically reduced. At the highest normalized field strength, the dominant frequency was approximately 4 kHz. Figure 30 presents the PSDs for thruster operation at 400V/8.3kW. The profiles in Fig. 30 indicate that the thruster dominant frequency is approximately 10 kHz for normalized magnetic field strength below 1.4. Increasing the magnetic field strength beyond 1.4 results in a secondary oscillation at ~70 kHz becoming more dominant, indicating that the thruster is starting to transition to a more oscillatory operating mode. Comparison of Figs. 29 and 30 indicate that at higher field strength, the TDU-1 thruster operating mode at 400 V is similar to the thruster mode at a discharge voltage of 300 V at lower field strength. Figure 31 presents the PSDs for thruster operation at 500V/10.4kW. Figure 31 indicates that the dominant frequency was 12-14 kHz for a normalized field of 1 and 1.2 but shifts to a higher frequency (~20 kHz) with a very pronounced high-energy peak at normalized field strengths above 1.2. Finally, Fig. 32 presents the PSDs for thruster operation at 600V/12.5kW. The PSDs in Fig. 32 indicate at the normalized field strength of 1.6 the thruster dominant frequency is ~50 kHz and that secondary oscillations at ~100 and 160 kHz appear.
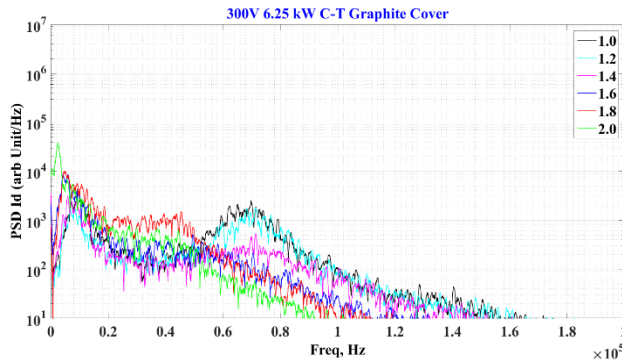
Figure 29. PSDs of TDU-1 discharge current at various magnetic fields for the graphite C-T configuration at 300V/6.25kW.
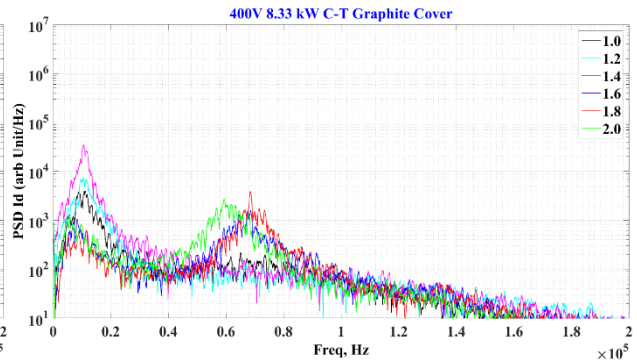
Figure 30. PSDs of TDU-1 discharge current at various magnetic fields for the graphite C-T configuration at 400V/8.33kW.
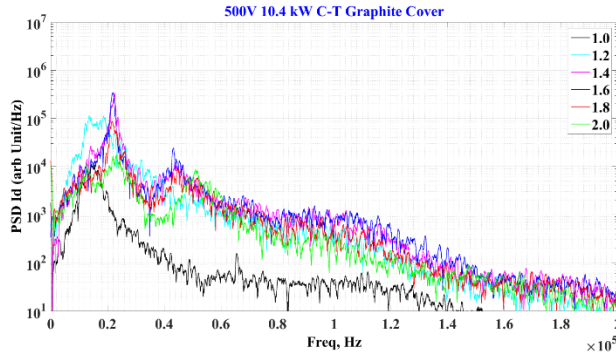
Figure 31. PSDs of TDU-1 discharge current at various magnetic fields for the graphite C-T configuration at 500V/10.4kW.
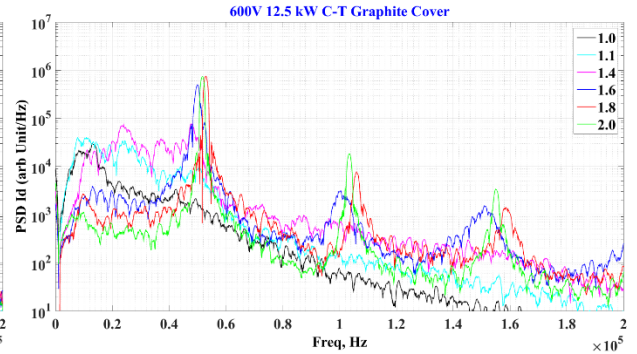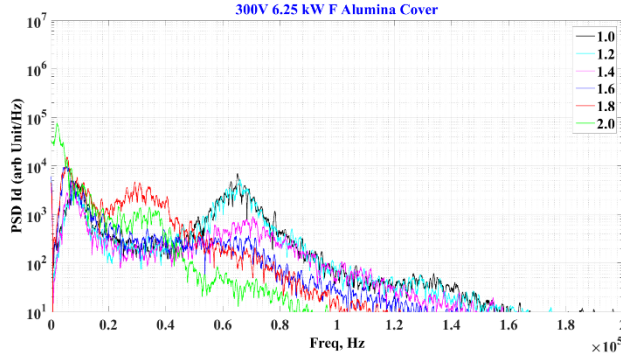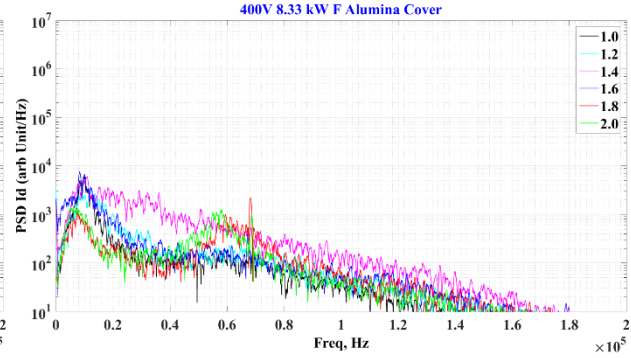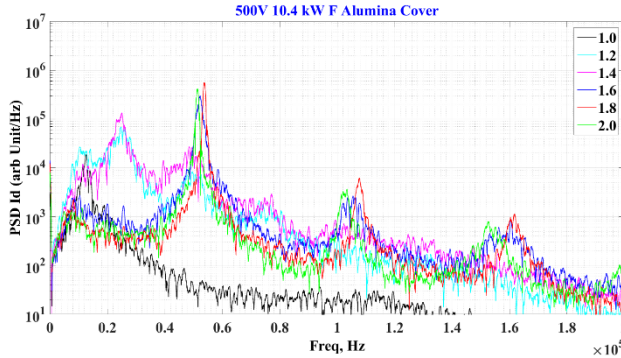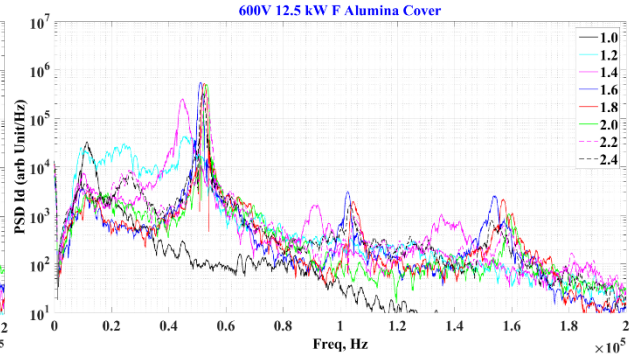
Figure 32. PSDs of TDU-1 discharge current at various magnetic fields for the graphite C-T configuration at 600V/12.5kW.

2. *Alumina Front Pole Cover Floating Thruster Configuration*

Figure 33 presents the PSDs for thruster operation at 300V/6.25 kW. The profiles in Fig. 33 are almost identical to what was presented in Fig. 29 for the graphite C-T configuration. Figure 34 presents the PSDs for thruster operation at 400V/8.3kW. The profiles in Fig. 34 are qualitatively similar to profiles presented in Fig. 30 with slightly lower oscillation levels. Figure 35 presents the PSDs for thruster operation at 500V/10.4kW, which presents trends that are qualitatively similar to Fig. 32 (graphite C-T at 600V/12.5kW). Results in Fig. 34 indicate that the thruster can operate at two distinct modes, a low oscillatory mode at a normalized magnetic field setting of 1.2 and a highly oscillatory mode at normalized magnetic field settings of 1.6 and above. At normalized magnetic field settings of 1.2 and 1.4, the thruster is in a transitional mode. Figure 36 presents the PSDs for 600V/12.5kW thruster operation, showing trends similar to Fig. 35.

Figure 33. PSDs of TDU-1 discharge current at various magnetic fields for the alumina F configuration at 300V/6.25kW.

Figure 34. PSDs of TDU-1 discharge current at various magnetic fields for the alumina F configuration at 400V/8.33kW.

Figure 35. PSDs of TDU-1 discharge current at various magnetic fields for the alumina F configuration at 500V/10.4kW.

Figure 36. PSDs of TDU-1 discharge current at various magnetic fields for the alumina F configuration at 600V/12.5kW.

V. Facility Background Pressure Effects Characterization of TDU-1 Thruster Operation

This section presents the experimental data from the facility background pressure effects characterization of the TDU-1 thruster. The key thruster operating parameters and measurements that will be presented in this section include total mass flow rate, total thruster efficiency, total specific impulse, normalized I_d-Pk2Pk, normalized I_d-RMS, PSDs, and IVB sweeps. For the pressure characterization tests, the facility background pressure was elevated by injection of additional xenon flow into VF-5's mid-section. The anode and cathode (7% of anode) mass flow rates were adjusted to maintain the prescribed thruster discharge power (i.e., adjust anode flow rate to maintain discharge current magnitude). For all the test conditions reported in this section, the magnetic field was set at a normalized nominal value of 1.6.

A. TDU-1 Thruster Performance and Stability

The TDU-1 thruster performance was characterized at various facility background pressure conditions for the graphite C-T and alumina F thruster configurations. Table 5 presents a summary of TDU-1 test conditions.

Table 5. Summary of the TDU-1 thruster tests conditions during the background pressure facility effects characterization test for the graphite C-T and alumina F configurations.

Thruster Operating Condition	Graphite C-T					Alumina F			
	Pressure, µTorr-Xe					Pressure, µTorr-Xe			
300 V, 1.8 kW	1.76	4.9	8.6	12	19.7	2	5	9	17
300 V, 6.25 kW	4.5	9.3	13.7	25		5	13	25	
400 V, 8.33 kW	4.5	9.4	12.5	25.5		5	13	25	
500 V, 10.4 kW	4.4	9.4	12.4	25.5		5	13	26	
600 V, 12.5 kW	4.6	9.2	12.7	25		4	13	25	

Figures 37 and 38 present the total mass flow rate variation with facility background pressure for the graphite C-T and alumina F thruster configurations, respectively. Figures 39 and 40 present the thrust variation with facility background pressure for the graphite C-T and alumina F thruster configurations, respectively. Results presented in Figs. 37 and 38 indicate that the mass flow rate decreases with increased facility background pressure. This has been observed previously with other Hall thrusters and is mainly attributed to the thruster ingestion of neutral background xenon, thus necessitating a reduction in the anode flow rate [16]. Figures 39 and 40 also indicate that the TDU-1 thrust, for the most part, decreased with increasing facility background pressure. This reduction in thrust is due to the reduced anode flow rate at elevated facility background pressure and matches trends found with other thrusters [37]. Inspection of Figs. 37-40 also indicates that for thruster operation at 300V/1.8kW at a thruster flow rate of ~6.4 mg/s, the rate of total mass flow rate and thrust reduction with increased facility background pressure is almost 3× that when the thruster is operating at a flow rate of approximately 20.5 mg/s. This indicates that the TDU-1 thruster is more sensitive to the facility background pressure at lower flow rates.
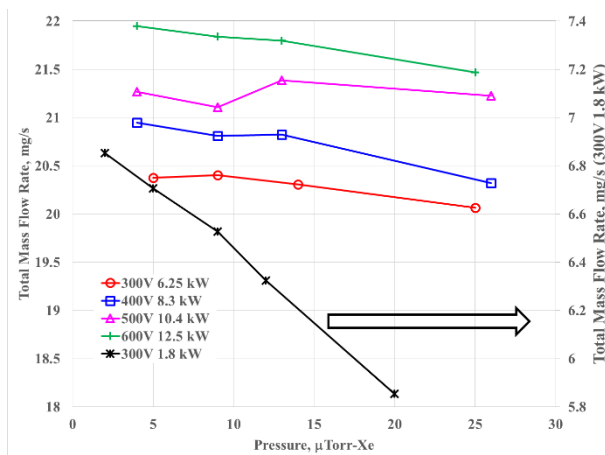

Figure 37. TDU-1 total mass flow rate variation with background pressure at selected thruster operating conditions for the graphite C-T front pole cover configuration.
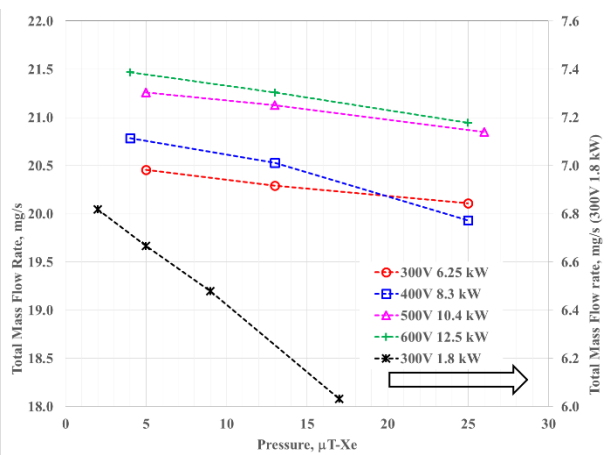
Figure 38. TDU-1 total mass flow rate variation with background pressure at selected thruster operating conditions for the alumina F front pole cover configuration.
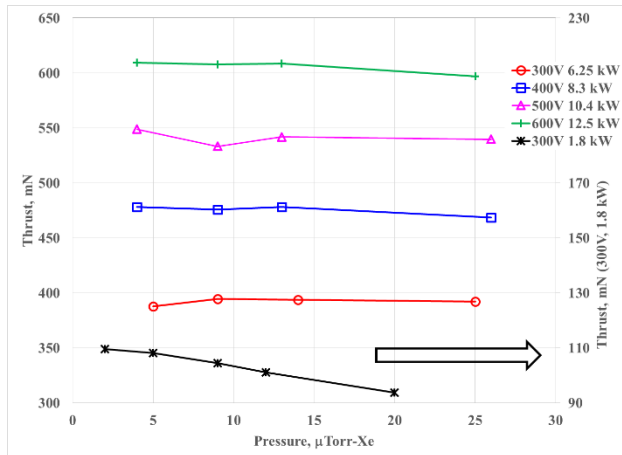
Figure 39. TDU-1 thrust variation with background pressure at selected thruster operating conditions for the graphite C-T front pole cover configuration.
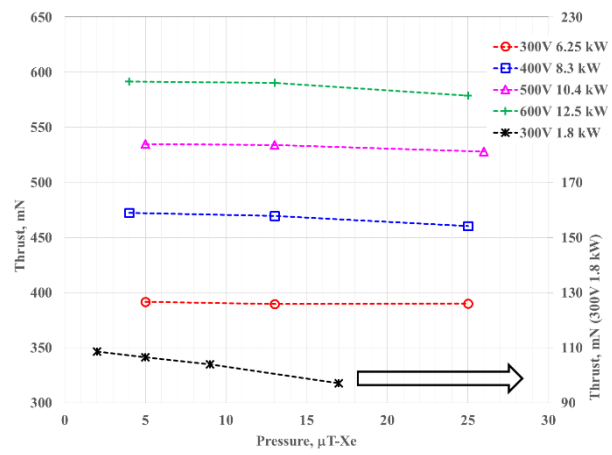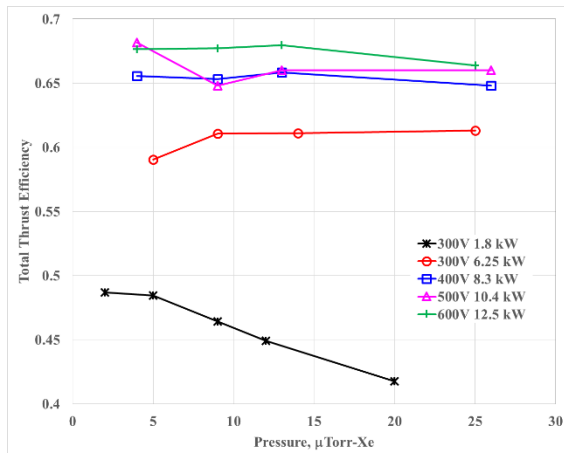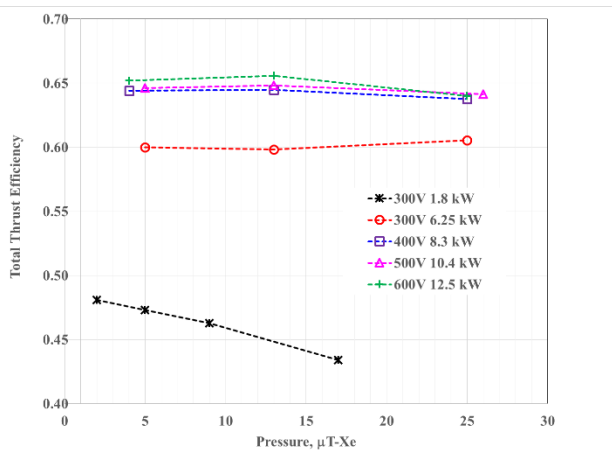
Figure 40. TDU-1 thrust variation with background pressure at selected thruster operating conditions for the alumina F front pole cover configuration.

Figures 41 and 42 present the total thrust efficiency variation with facility background pressure for the graphite C-T and alumina F thruster configurations, respectively. Figures 43 and 44 present the total specific impulse variation with facility background pressure for the graphite C-T and alumina F thruster configurations, respectively. Results in Figs. 41 and 42 indicate that, in general, the total thrust efficiency is almost constant (within uncertainty of measurements) with increased facility background pressure except at 300V/1.8kW. However, results in Figs. 43 and 44 indicate that the TDU-1 total specific impulse increases very slightly with increased facility background pressure. This is an indication that the thrust is decreasing at a slower rate than the thruster's mass flow (or that increasing the facility pressure results in a steeper decline in the thruster's mass flow rate when compared to the measured thrust).

Figure 41. TDU-1 total thruster efficiency variation with background pressure at selected thruster operating conditions for the graphite C-T front pole cover configuration.

Figure 42. TDU-1 total thruster efficiency variation with background pressure at selected thruster operating conditions for the alumina F front pole cover configuration.

Figures 45 and 46 present the normalized discharge current Pk2Pk variation with facility background pressure for the graphite C-T and alumina F thruster configurations, respectively. Figures 47 and 48 present the normalized discharge current RMS variation with facility background pressure for the graphite C-T and alumina F thruster configurations, respectively. Results in Figs. 45-48 indicate that, in general, for both thruster configurations the normalized discharge current Pk2Pk and RMS increased with increased facility background pressure. Thus for the TDU-1 thruster configurations, increased facility background pressure resulted in a slightly more oscillatory discharge.
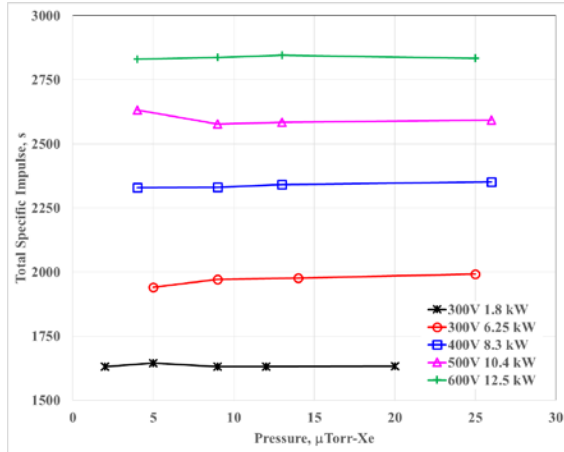
Figure 43. TDU-1 total specific impulse variation with background pressure at selected thruster operating conditions for the graphite C-T front pole cover configuration.
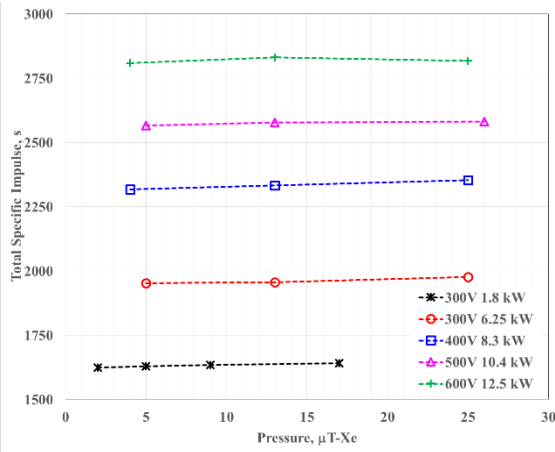

Figure 44. TDU-1 total specific impulse variation with background pressure at selected thruster operating conditions for the alumina F front pole cover configuration.
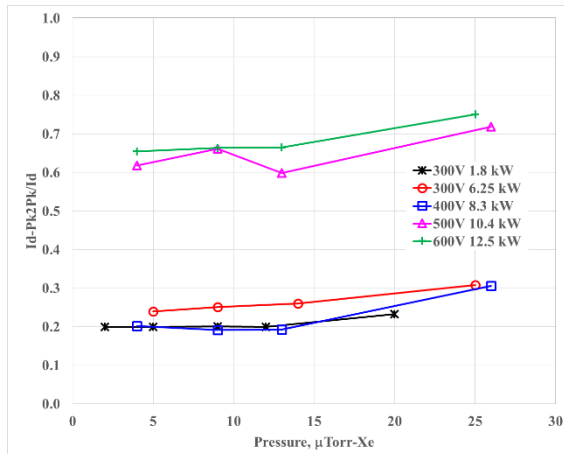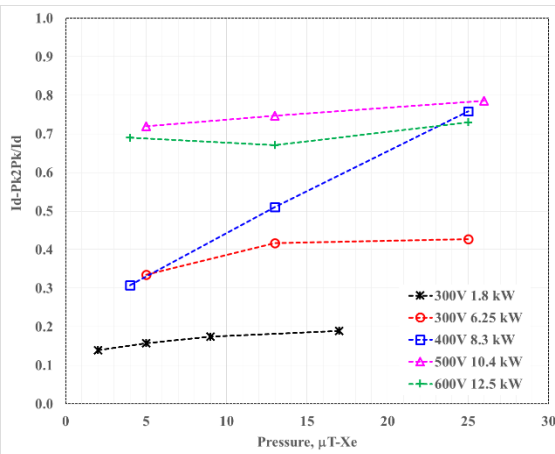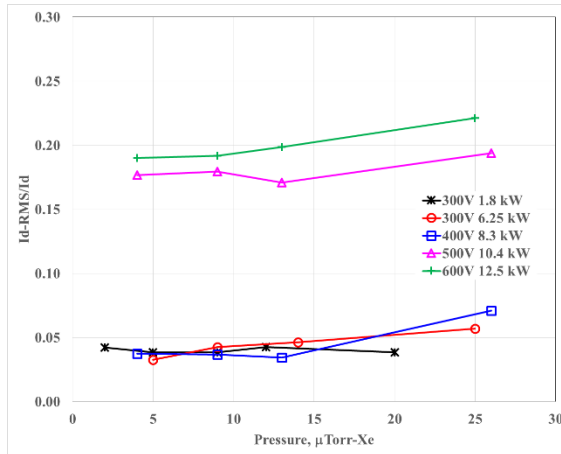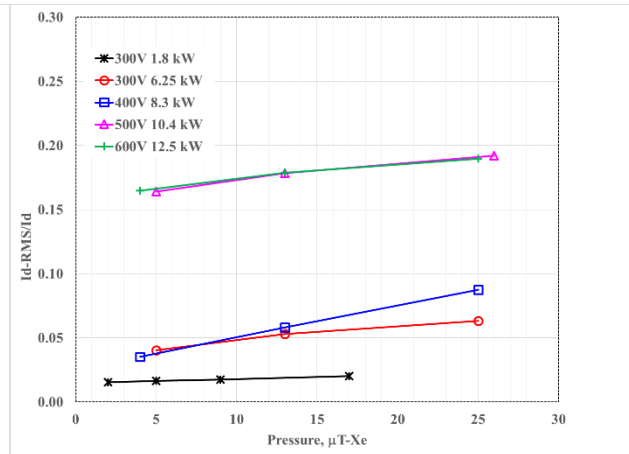

Figure 45. TDU-1 normalized Id-Pk2Pk variation with background pressure at selected thruster operating conditions for the graphite C-T front pole cover configuration.

Figure 46. TDU-1 normalized Id-Pk2Pk variation with background pressure at selected thruster operating conditions for the alumina F front pole cover configuration.

Figure 47. TDU-1 normalized Id-RMS variation with background pressure at selected thruster operating conditions for the graphite C-T front pole cover configuration.

Figure 48. TDU-1 normalized Id-RMS variation with background pressure at selected thruster operating conditions for the alumina F front pole cover configuration.

Analysis of the TDU-1 PSDs for TDU-1 operating at the conditions listed in Table 5 confirms the same trends found in Figs. 29-36 and reveals some additional trends with the increased facility background pressure. Figures 49-57 present the PSDs for the TDU-1 thruster operating at the lowest facility background pressure and at elevated background pressure for various thruster operating conditions. In general, it is observed that the peak PSD increases with increased facility background pressure and that the location of the peak shifts to a higher frequency. The increase in the peak PSD magnitude indicates an increase in the discharge current Pk2Pk.

Figures 49 and 50 present the PSDs for the 300V/1.8kW operation for both thruster configurations. The magnitude of the PSDs are relatively small due to the quiescent and low discharge current operation of the thruster. Figures 51 and 52 present the PSDs at 300V/6.25kW thruster operation for both thruster configurations. The dominant frequency occurs at approximately 6 kHz with a secondary frequency at approximately 70 kHz. The PSD magnitude of the secondary frequency increases with elevated background pressure, but the magnitude is still lower than the dominant frequency, which is an indication that the discharge is becoming more oscillatory but has not transitioned to another mode. Figures 53 and 54 present the PSDs for thruster operation at 400 V and 8.3 kW. Results in Fig. 53 indicate that for the graphite C-T thruster configuration, the thruster oscillatory behavior did not change up to a facility background pressure of 13 µTorr-Xe. However, at a facility background pressure of 25.5 µTorr-Xe the dominant frequency PSD magnitude increased and the secondary oscillation was damped. Results in Fig. 54 indicate that for the alumina F thruster configuration, the magnitude of the PSD increased with increasing pressure and that no dominant secondary oscillations occurred during operation at 400 V.
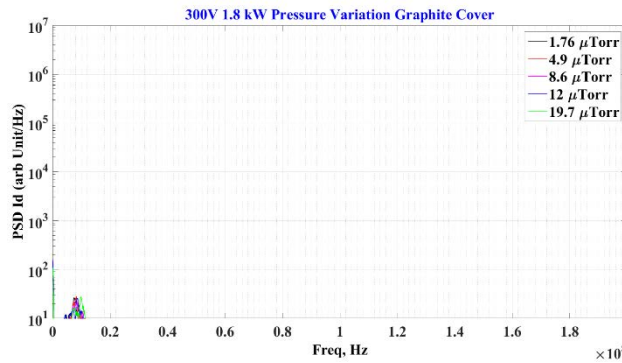

Figure 49. PSDs of TDU-1 discharge current at various magnetic fields for the graphite C-T configuration at 300V/1.8kW.
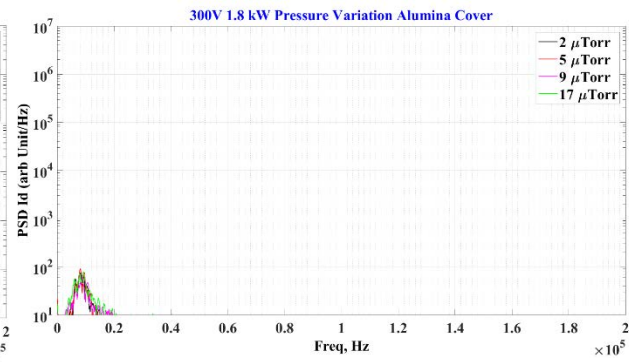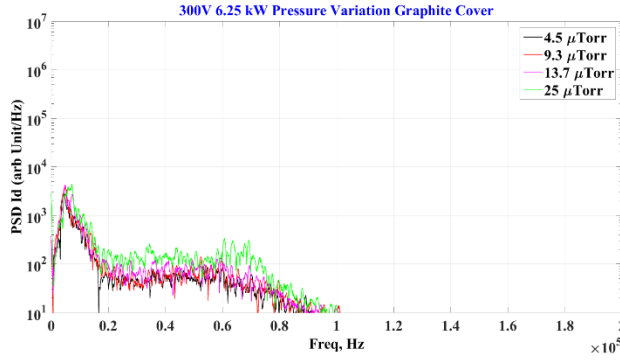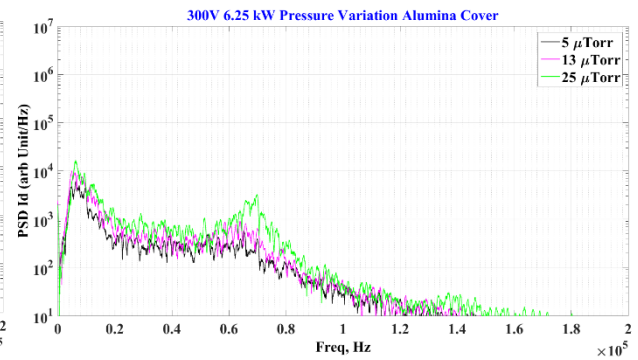
Figure 50. PSDs of TDU-1 discharge current at various magnetic fields for the alumina F configuration at 300V/1.8kW.

20
American Institute of Aeronautics and Astronautics

Figures 55 and 56 present the PSDs for the 500V/10.4kW operation for both thruster configurations. For the graphite C-T thruster configuration, results in Fig. 55 indicate that at a facility background pressure of 25.5 µTorr-Xe, the thruster was operating in a mode that was different than at a facility background pressure of 12.4 µTorr-Xe and lower. For the alumina F configuration, PSD profiles shown in Fig. 56 indicate that the thruster was operating in the same mode at all facility background pressure conditions. Increase in the facility background pressure resulted in a slight increase in the PSD magnitude and an increase in the corresponding frequencies.

Figures 57 and 58 present the PSDs for the 600V/12.5kW operation for both thruster configurations. Results in Figs. 57 and 58 indicate similar PSD profiles and trends for both configurations. The trends presented in Figs. 57 and 58 show that the thruster was operating in the same mode at all facility background pressure conditions for both configurations; increasing the facility background pressure resulted in a slight increase in the PSD magnitude and an increase in the corresponding frequencies (i.e., PSD shifted to the right).

Figure 51. PSDs of TDU-1 discharge current at various magnetic fields for the graphite C-T configuration at 300V/6.25kW.

Figure 52. PSDs of TDU-1 discharge current at various magnetic fields for the alumina F configuration at 300V/6.25kW.
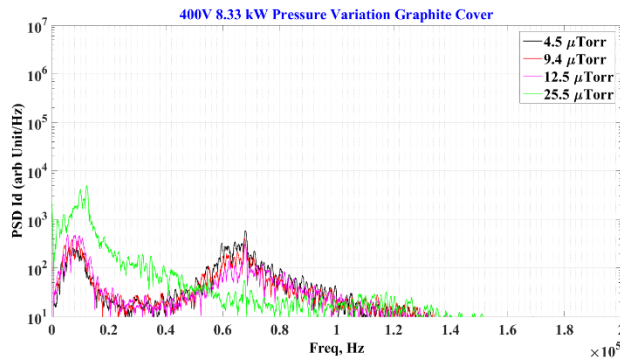

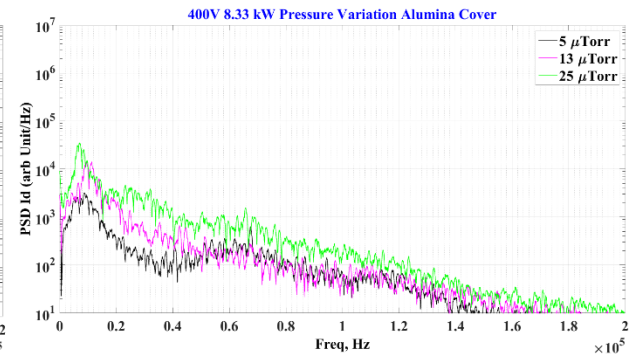**Figure 53. PSDs of TDU-1 discharge current at varying magnetic fields for the graphite C-T configuration at 400V/8.33kW.**

Figure 54. PSDs of TDU-1 discharge current at varying magnetic fields for the alumina F configuration at 400V/8.33kW.

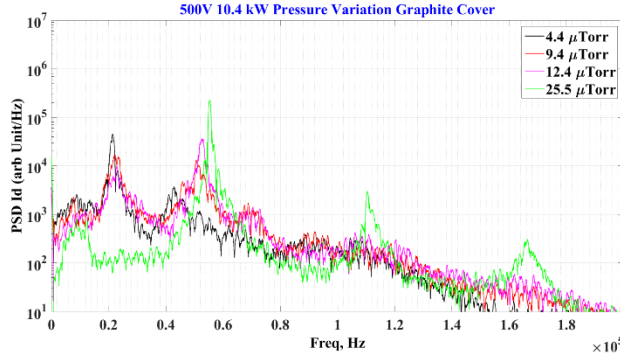American Institute of Aeronautics and Astronautics

Figure 55. PSDs of TDU-1 discharge current at various magnetic fields for the graphite C-T configuration at 500V/10.4kW.
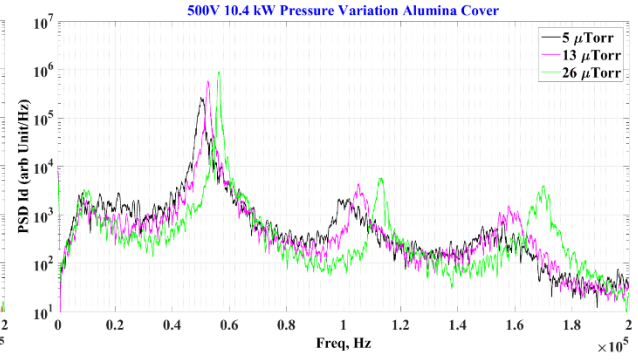

Figure 56. PSDs of TDU-1 discharge current at various magnetic fields for the alumina F configuration at 500V/10.4kW.
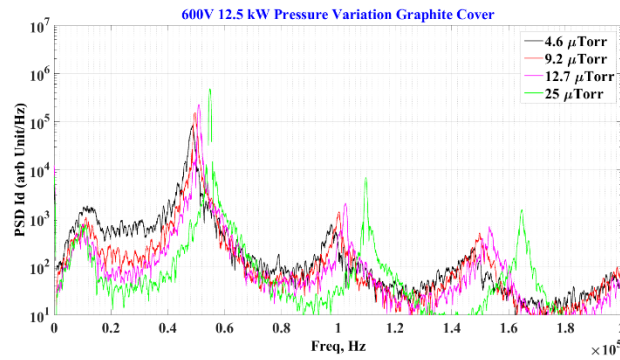

Figure 57. PSDs of TDU-1 discharge current at various magnetic fields for the graphite C-T configuration at 600V/12.5kW.
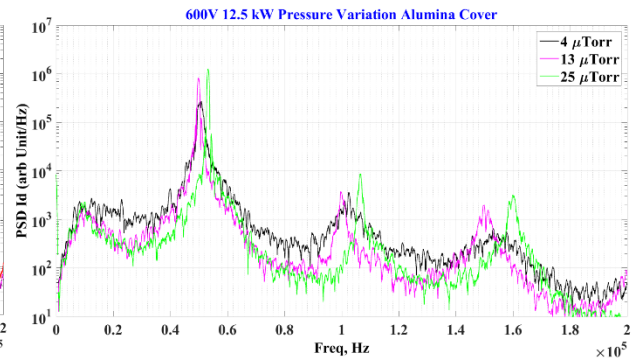

Figure 58. PSDs of TDU-1 discharge current at various magnetic fields for the alumina F configuration at 600V/12.5kW.

B. Current-Voltage-Magnetic Field Sweeps with Varying Facility Background Pressure

As part of the facility background pressure effects characterization tests, IVB sweeps were performed at different facility background pressure conditions. Table 6 summarizes the background pressure conditions during the IVB sweeps. In this section, only the IVBs at the 20.5 and 20.2 mg/s for the thruster graphite C-T and alumina F configurations, respectively, will be presented. The IVBs for the test conditions highlighted in grey are presented in Appendix A. Figures 59-64 present the IVBs for the 20.5 mg/s graphite C-T and 20.2 mg/s alumina F (highlighted in green in Table 6). The IVBs, for both thruster configurations, at the three different background pressure conditions qualitatively show similar profiles. Increasing the background pressure resulted in a slight change in the normalized discharge current RMS, and the increased pressure did not change when the thruster was transitioning to a more oscillatory mode (typically it occurred above a discharge voltage of 400 V). For the graphite C-T thruster configuration results presented in Appendix A, it is observed that at flow rates of 6.4. 9.8, 15.3, and 18.4 mg/s the discharge became slightly more oscillatory as the VF-5 background pressure was increased. These results indicate that the impact of increased facility background pressure depends on the thruster's flow rate. The higher the thruster's flow rate, the more invariant the thruster's discharge is to the increased facility background pressure.

Table 6. VF-5 background pressure conditions during the IVB sweeps at the various thruster operating anode flow rates for both thruster configurations.

Thruster Flow Rate, mg/s	Graphite C-T		
	Pressure, μTorr-Xe		
	LP	MP	HP
6.4	1.8	5.5	11.2
9.8	2.7	7.5	14.5
15.3	4.0	11.0	21.8
18.4	4.1	13.4	25.7
19.3	5.0	14.4	24.4
20.5	5.1	16.2	24.7
21.0	4.6		
21.5	4.8		
21.9	5.0		
22.5	5.1	18.5	27.7
	Alumina F		
	Pressure, μTorr-Xe		
	LP	MP	HP
6.4	1.8		
20.2	4.5	13.1	25.8
22.5	4.9		
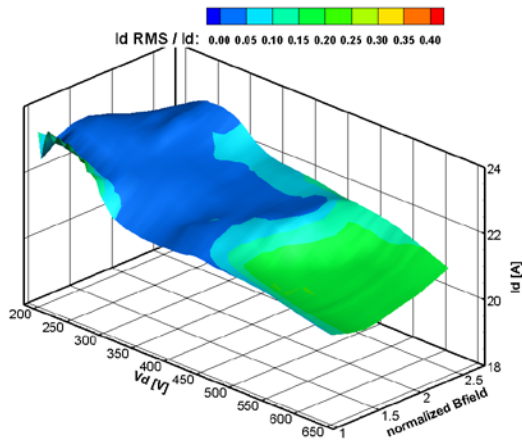
Figure 59. IVB map of normalized Id-RMS at 20.5 mg/s for the graphite cover C-T thruster configuration at a background pressure of 5.1 μTorr-Xe.
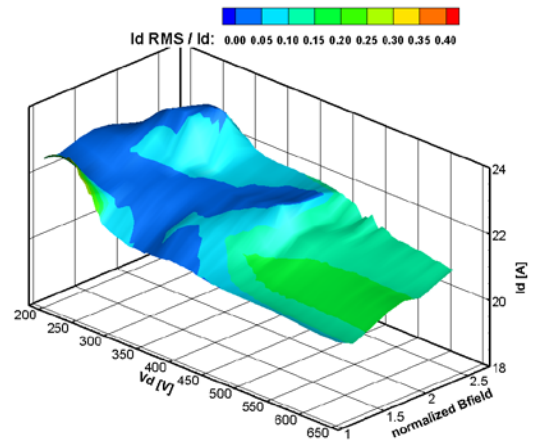
Figure 60. IVB map of normalized Id-RMS at 20.22 mg/s for the alumina cover F thruster configuration at a background pressure of 4.45 μTorr-Xe.
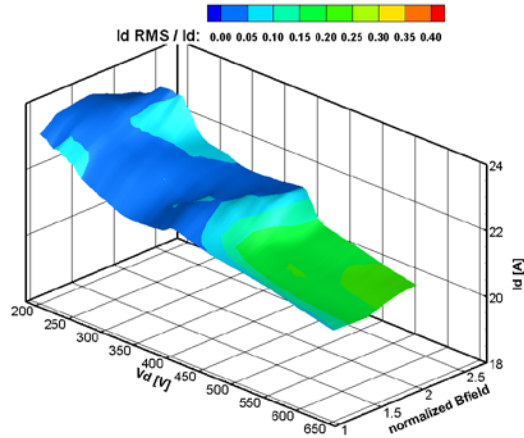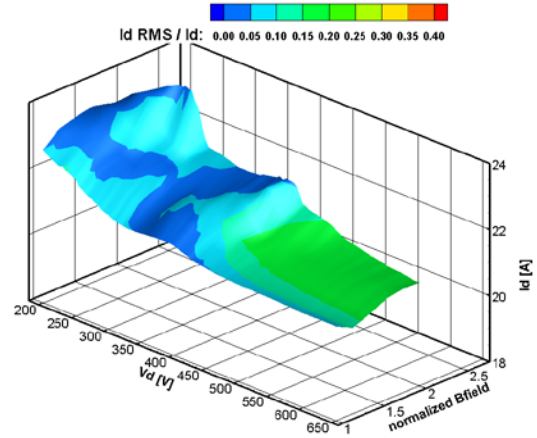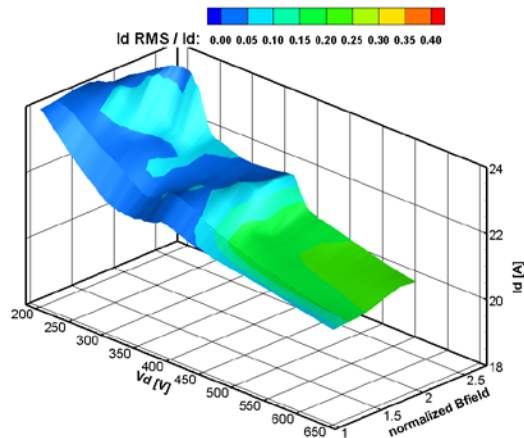
American Institute of Aeronautics and Astronautics

Figure 61. IVB map of normalized Id-RMS at 20.5 mg/s for the graphite cover C-T thruster configuration at a background pressure of 16.2 µTorr-Xe.
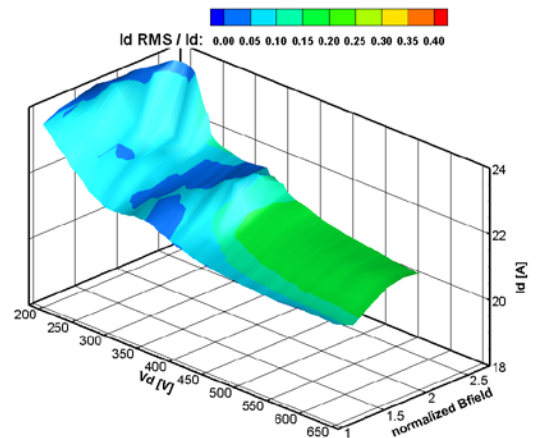

Figure 62. IVB map of normalized Id-RMS at 20.22 mg/s for the alumina cover F thruster configuration at a background pressure of 13.1 µTorr-Xe.

Figure 63. IVB map of normalized Id-RMS at 20.5 mg/s for the graphite cover C-T thruster configuration at a background pressure of 24.7 µTorr-Xe.

Figure 64. IVB map of normalized Id-RMS at 20.22 mg/s for the alumina cover F thruster configuration at a background pressure of 25.8 µTorr-Xe.

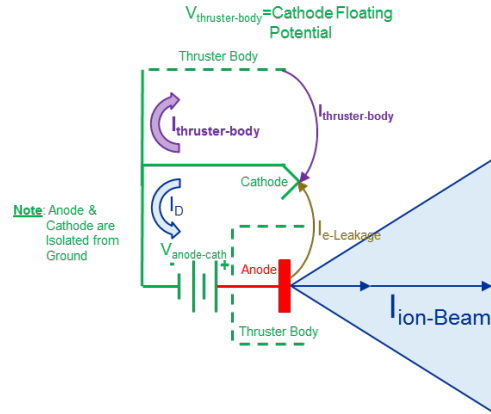American Institute of Aeronautics and Astronautics

VI. Discussion

Results reported in this paper summarized the performance of two TDU-1 thruster configurations: a configuration with a graphite front pole cover with the thruster electrically tied to cathode and a configuration with an alumina front pole cover and the thruster body floating. Characterization of the two configurations reveals that there are two key differences: conducting vs. dielectric front pole cover material; and two different electrical configurations, with the thruster tied to cathode and with the thruster floating.

Tests on the TDU-1 thruster at 600V/12.5kW with the graphite pole covers revealed that floating the thruster body resulted in negative thruster potentials (up to – 45 V) and very large negative AC components (up to -126 V Pk2Pk). The large negative thruster body potentials (DC and AC) would result in front pole cover erosion rates that would have drastically reduced the thruster's life capability. Electrically tying the thruster body's to cathode greatly improved the thruster body voltage to -9 V from -45 V and its associated Pk2Pk to -36 V from -126 V. In the C-T configuration a thruster body current of ~1.8 A was measured. It is stipulated that additional electron current is being conducted through the front pole covers and causes a change in the thruster's ionization and acceleration zones structure. Figure 65 illustrates C-T circuit diagram. The C-T configuration does result in electrons still being collected by the thruster body; however, because the thruster body is electrically connected to the cathode, the collected electrons are forced back through the hollow cathode [39], which is confirmed by the fact that the current measured on the cathode return line was ~22.6 A (20.8 A +1.8 A). Also, to operate at 12.5 kW in the C-T configuration necessitated increasing the anode flow rate by 2.1% over its value when the thruster was floated. Finally, the thruster's performance increased by approximately 3% for the C-T configuration when compared to the F configuration. The improved thruster performance is partly attributed to the higher mass flow rate resulting in higher thrust which is an indication of improved mass utilization.

$$I_{Discharge} = I_{ion-Beam} + I_{e-Leakage}$$

$$I_{Cathode} = I_{ion-Beam} + I_{e-Leakage} + I_{Thruster-Body}$$

Thruster Body Tied to Cathode Common

Figure 65. A partial circuit diagram of the thruster body electrically tied to the cathode common.
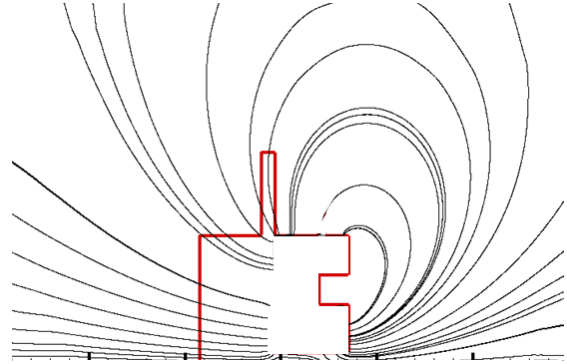

Figure 66. Illustration of TDU-1 magnetic field streamlines.

For the alumina thruster configuration, changing the thruster's electrical configuration did not impact the thruster performance [8]. The thruster's performance levels (for all three electrical configurations) were almost identical to what was measured in 2015 on TDU-1.[13] It is stipulated that for the dielectric thruster configuration and for operation in the C-T or GND configuration, current collection does not take place at the front poles (as is the case for the graphite front pole covers) but occurs at exposed thruster conducting surfaces. This is illustrated in Fig. 66 which shows that TDU-1 thruster magnetic field lines terminate at conducting surfaces (i.e., outer core, backpole, and radiator).

It is important to note that at the lowest attainable background pressure conditions, the graphite C-T configuration was slightly noisier than the alumina F. Slightly higher Pk2Pk and RMS discharge current magnitudes were measured for the graphite C-T configuration as was presented in Figs 18 and 19. However, the global thruster oscillatory mode for the two configurations was very similar, and the thruster operated stably in both configurations.

The facility background pressure characterization tests revealed that the background pressure affects the thruster's performance, discharge current oscillation characteristics, and the IVB maps, but the change in those measured values is not very large. Tests of both thruster configurations at elevated background pressure conditions at flow rates of ~

20.5 mg/s found that increasing the facility background pressure results in higher magnitude oscillations. Thus, for the TDU-1 thruster, which is a magnetically shielded thruster with centrally mounted cathode, operation at a background pressure of ~4 μTorr-Xe results in less oscillatory thruster operation than at higher background pressures. This was further confirmed by the PSD analysis of the discharge current waveforms which found that higher peaks were attained at higher pressure and that the dominant frequency magnitude increased slightly with facility background pressure. Finally, the IVB sweep results also showed that increased facility background pressure did not alter the qualitative form of the IVB profile. The IVB sweeps showed that the thruster changes modes at voltages above 400 V which is consistent with the Pk2Pk and RMS plots. The IVBs also indicated that the thruster oscillations grew slightly with increased facility background pressure. These findings are particular to the TDU-1 thruster configuration because other thrusters have shown that higher facility background pressures result in a less oscillatory thruster operation.[28,30] Also tests at elevated facility pressure indicate a similar behavior to what was observed with the H6MS thruster when the cathode was located along the thruster's centerline.[31] To better understand why the TDU-1 thruster was more "stable" at lower facility background pressure requires performing more detailed tests at 10 and 15 mg/s, including implementation of near and far field-plume plasma diagnostics.

VII. Summary and Future Work

NASA's Hall Effect Rocket with Magnetic Shielding (HERMeS) 12.5 kW TDU-1 has been the subject of extensive technology maturation in preparation for flight system development. A number of tests were performed on the thruster, and this paper present results from a subset of the characterization tests.

Part of the technology maturation effort included an evaluation of thruster operation with conducting and dielectric front pole cover materials in two different electrical configurations. A graphite front pole cover thruster configuration with the thruster body electrically tied to cathode and an alumina front pole cover thruster configuration with the thruster body floating were evaluated. Performance characterization tests found that higher thruster performance was attained with the graphite front pole cover configuration and the thruster electrically tied to cathode. A total thrust efficiency of 68% and a total specific impulse of 2,820 s were demonstrated at a discharge voltage of 600 V and a discharge power of 12.5 kW. Thruster stability regimes were characterized with respect to the thruster discharge current oscillations (discharge current Pk2Pk and RMS magnitudes), along with maps of the current-voltage-magnetic field (IVB). Analysis of TDU-1 discharge current waveforms found that slightly lower normalized discharge current Pk2Pk and RMS magnitudes were attained when the thruster was electrically floated with alumina front pole covers.

In addition, both configurations were evaluated at different facility pressure conditions to determine effects on thruster operation. Thruster performance and stability were shown to be mostly invariant to changes in the facility background pressure for pressures below 1×10^{-5} Torr-Xe (for thruster flow rates of 20.2 mg/s and above). Power spectral density analysis of the discharge current waveforms found that increasing the background pressure resulted in a higher discharge current dominant frequency with the PSD profiles shifting to the right with increased facility background pressure. Finally, the IVB maps of the TDU-1 thruster at elevated background pressures showed that the discharge current became more oscillatory at lower thruster mass flow rates and that thruster operation at higher flow rates resulted in less change to the thruster's IVB characteristics.

Future work on the thruster includes additional tests to be able to extrapolate the projected thruster performance and stability to zero-pressure. This includes performing tests at thruster flow rates of 10 and 15 mg/s at elevated facility background pressure conditions. In addition, analysis of the data that was acquired during this test campaign is ongoing. The analyses include looking at other thruster operating parameters such as discharge voltage oscillations, cathode-to-ground voltage, thruster body voltage, thruster body current, and other thruster telemetry to gain more insights on how the thruster operation changes at the various thruster background pressure conditions.
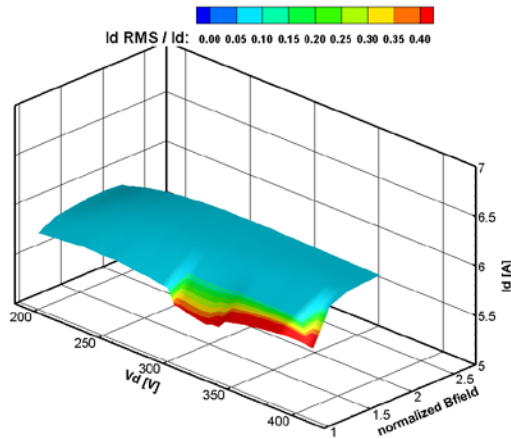
Figure 67. IVB map of normalized Id-RMS at 6.45 mg/s for the graphite cover C-T thruster configuration at a background pressure of 1.8 µTorr.
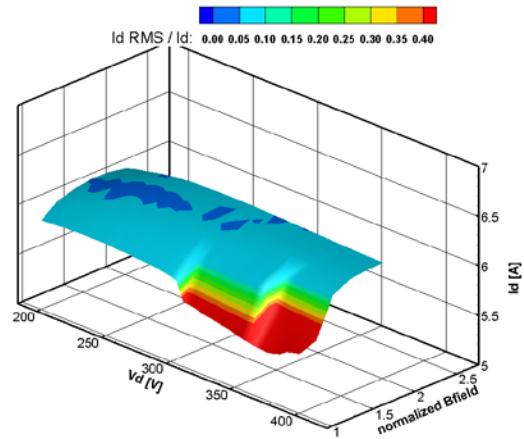

Figure 68. IVB map of normalized Id-RMS at 6.45 mg/s for the graphite cover C-T thruster configuration at a background pressure of 5.5 µTorr.
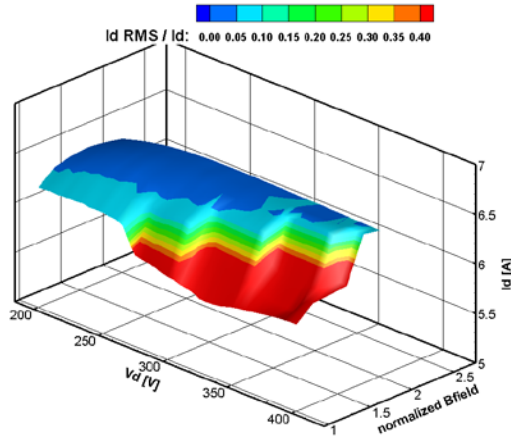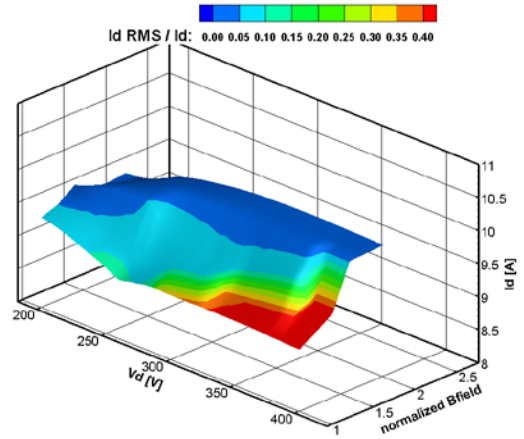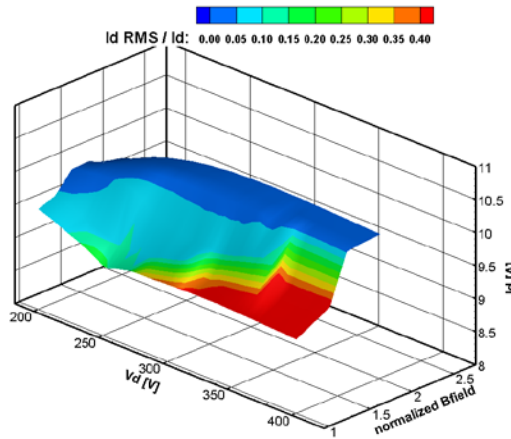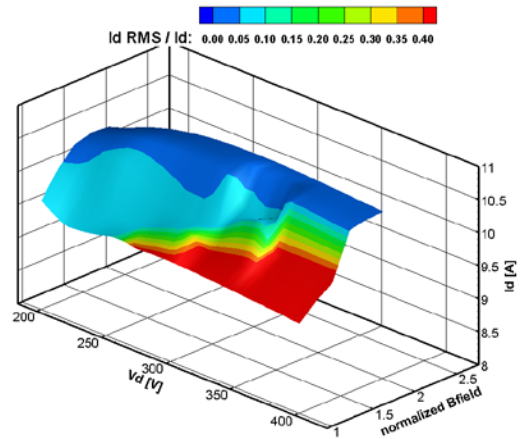

Figure 69. IVB map of normalized Id-RMS at 6.45 mg/s for the graphite cover C-T thruster configuration at a background pressure of 11.2 µTorr.

Figure 70. IVB map of normalized Id-RMS at 9.83 mg/s for the graphite cover C-T thruster configuration at a background pressure of 2.7 µTorr.

Figure 71. IVB map of normalized Id-RMS at 9.83 mg/s for the graphite cover C-T thruster configuration at a background pressure of 7.5 µTorr.

Figure 72. IVB map of normalized Id-RMS at 9.83 mg/s for the graphite cover C-T thruster configuration at a background pressure of 14.5 µTorr.
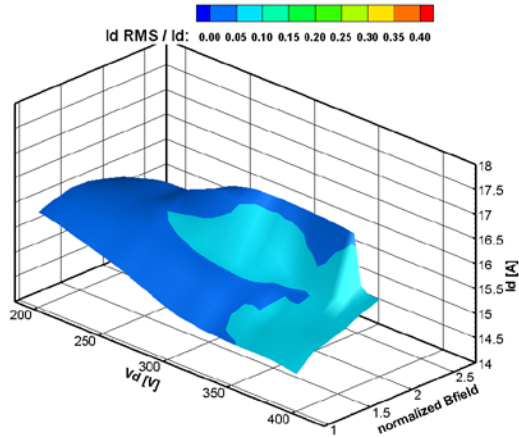
27

Figure 73. IVB map of normalized Id-RMS at 15.33 mg/s for the graphite cover C-T thruster configuration at a background pressure of 4 µTorr-Xe.
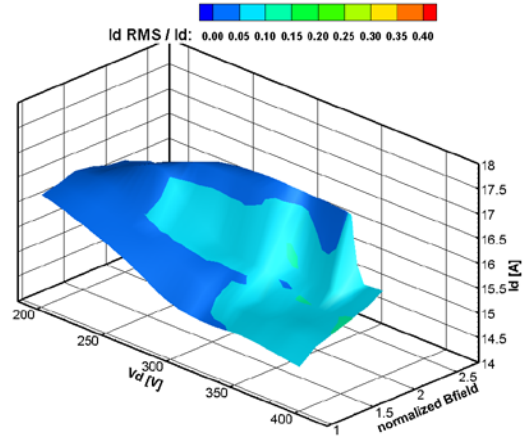

Figure 74. IVB map of normalized Id-RMS at 15.33 mg/s for the graphite cover C-T thruster configuration at a background pressure of 11 µTorr-Xe.
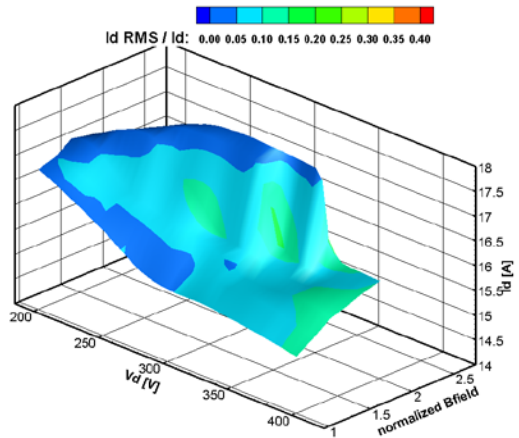

Figure 75. IVB map of normalized Id-RMS at 15.33 mg/s for the graphite cover C-T thruster configuration at a background pressure of 21.8 µTorr-Xe.
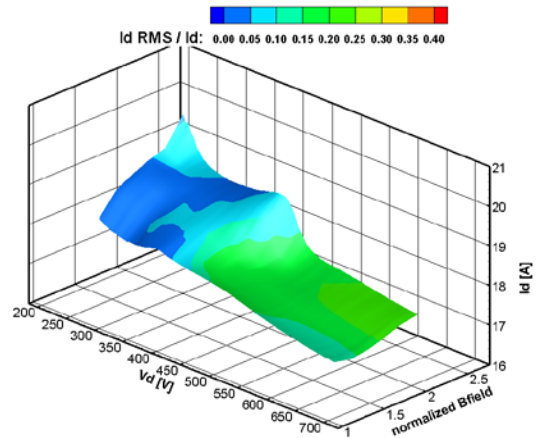

Figure 76. IVB map of normalized Id-RMS at 18.38 mg/s for the graphite cover C-T thruster configuration at a background pressure of 4.1 µTorr-Xe.
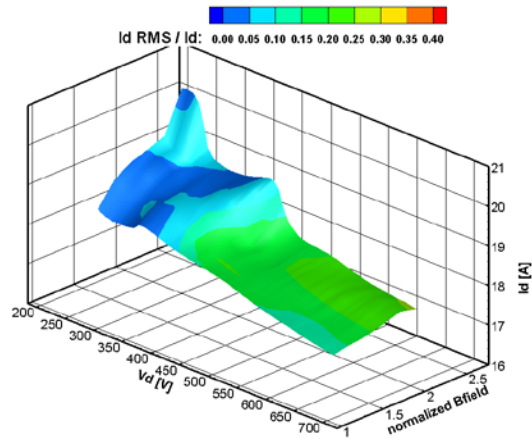

Figure 77. IVB map of normalized Id-RMS at 18.38 mg/s for the graphite cover C-T thruster configuration at a background pressure of 13.4 µTorr-Xe.
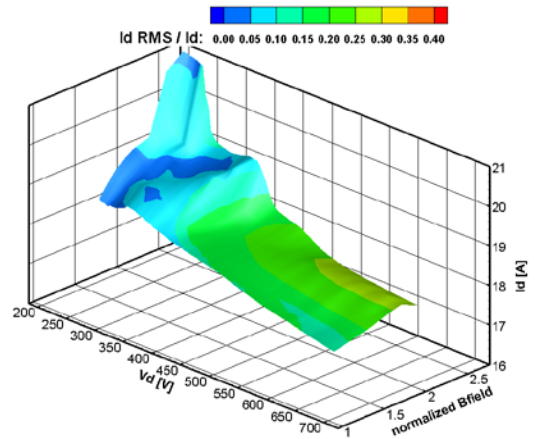

Figure 78. IVB map of normalized Id-RMS at 18.38 mg/s for the graphite cover C-T thruster configuration at a background pressure of 25.7 µTorr-Xe.
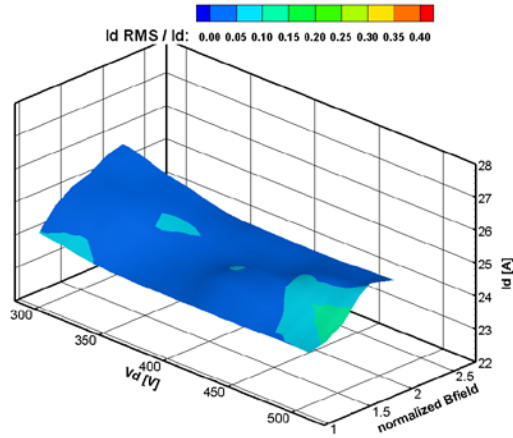
Figure 79. IVB map of normalized Id-RMS at 22.54 mg/s for the graphite cover C-T thruster configuration at a background pressure of 5.05 µTorr-Xe.
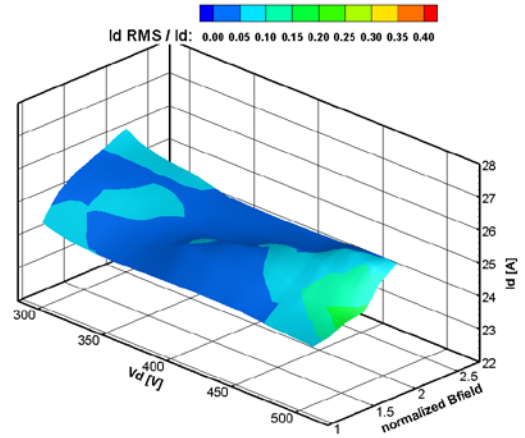

Figure 80. IVB map of normalized Id-RMS at 22.54 mg/s for the graphite cover C-T thruster configuration at a background pressure of 18.5 µTorr-Xe.
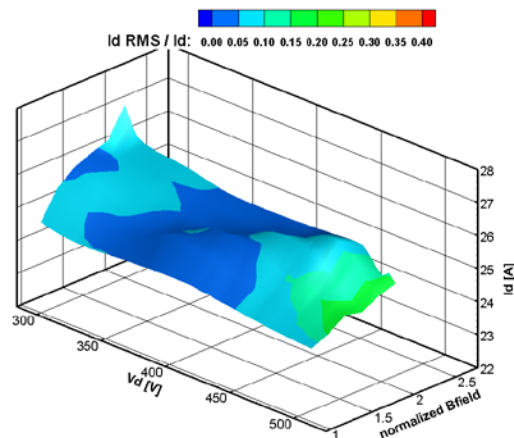

Figure 81. IVB map of normalized Id-RMS at 22.54 mg/s for the graphite cover C-T thruster configuration at a background pressure of 27.7 µTorr-Xe.

American Institute of Aeronautics and Astronautics

Acknowledgments

References

[1] B. K. Smith, M. L. Nazario, and C. C. Cunningham, "Solar Electric Propulsion Vehicle Demonstration to Support Future Space Exploration Missions," presented at the Space Propulsion 2012, Bordeaux, France, 2012.

[2] D. H. Manzella and K. Hack, "High-Power Solar Electric Propulsion for Future NASA Missions," presented at the 50th AIAA/ASME/SAE/ASEE Joint Propulsion Conference, Cleveland, OH, 2014.

[3] H. Kamhawi, W. Huang, T. W. Haag, J. Yim, L. Chang, L. Clayman, *et al.*, "Overview of the Development of the Solar Electric Propulsion Technology Demonstration Mission 12.5-kW Hall Thruster," presented at the 50th AIAA/ASME/SAE/ASEE Joint Propulsion Conference, Cleveland, OH, 2014.

[4] B. Spence, S. White, M. LaPointe, R. Takeda, G. Carter, K. Schmid, *et al.*, "Technology Maturation and Advancement Update of the ROSA/MegaROSA Solar Array " presented at the Space Power Workshop, Huntington Beach, CA, 2014.

[5] C. R. Mercer and et. al., "Solar Array Technology Development for Electric Propulsion," presented at the Space Power Workshop, Huntington Beach, CA, 2015.

[6] D. Murphy, M. Eskenazi, J. Spink, M. McEachen, T. Trautt, and M. McClenathen, "MegaFlex Solar Array Development and Test – Results from Phase 1 of the NASA Game Changing Development (GCD) Program for Solar Electric Propulsion (SEP) Solar Array Systems (SAS) Program," presented at the Space Power Workshop, Huntington Beach, CA, 2014.

[7] T. W. Kerslake, "Advanced Solar Arrays for NASA Electric Propulsion Missions," presented at the SciTech 2015, Kissimmee, FL, 2015.

[8] R. Brophy and B. Muirhead, "Near-Earth Asteroid Retrieval Mission (ARM) Study," presented at the 33rd International Electric Propulsion Conference, Washington, DC, 2013.

[9] M. Gates, "NASA's Asteroid Redirect Mission Concept Development Summary," presented at the IEEE Aerospace Conference, Big Sky, MT, 2015.

[10] B. Muirhead and J. R. Brophy, "Asteroid Redirect Robotic Mission Feasibility Study," presented at the Presented at teh IEEE Aerospace Conference, Big Sky, MT, 2014.

[11] D. D. Mazanek, R. G. Merrill, S. P. Belbin, D. M. Reeves, K. D. Earle, B. J. Naasz, *et al.*, "Asteroid Redirect Robotic Mission: Boulder Capture Overview Option," presented at the 50th AIAA/ASME/SAE/ASEE Joint Propulsion Conference, Cleveland, OH, 2014.

[12] N. Strange, D. Landau, T. Mcelrath, G. Lantoine, T. Lam, M. McGuire, *et al.*, "Overview of Mission Design for NASA Astreroid Redirect Robotic Mission Concept," presented at the 33rd International Electric Propulsion Conference, Washington, DC, 2013.

[13] H. Kamhawi, W. Huang, T. Haag, R. Shastry, R. Thomas, J. Yim, *et al.*, "Performance and Facility Background Pressure Characterization Tests of NASA's 12.5-kW Hall Effect Rocket with Magnetic Shielding Thruster," in *34th International Electric Propulsion Conference, IEPC-2015-07*, Hyogo-Kobe, Japan, 2015.

[14] R. Shastry, W. Huang, and H. Kamhawi, "Near-Surface Plasma Characterization of the 12.5-kW NASA TDU1 Hall Thruster," in *51st Joint Propulsion Conference*, ed. Orlando, FL, 2015.

[15] P. Peterson, H. Kamhawi, W. Huang, J. Yim, D. Herman, G. Williams, J. Gilland, and R. Hofer, "NASA HERMeS Hall Thruster Electrical Configuration Characterization," presented at the 52nd AIAA/SAE/ASEE Joint Propulsion Conference, Salt Lake City, UT, 2016.

[16] J. Myers, H. Kamhawi, J. Yim, and L. Clayman, "Hall Thruster Modeling and Test Data Correlation," presented at the 52nd AIAA/SAE/ASEE Joint Propulsion Conference, Salt Lake City, UT, 2016.

[17] G. J. Williams, J. H. Gilland, P. Y. Peterson, H. Kamhawi, W. Huang, M. Swiatek, *et al.*, "Wear Testing of the HERMeS Thruster," presented at the 52nd AIAA/SAE/ASEE Joint Propulsion Conference, Salt Lake City, UT, 2016.

[18] W. Huang, H. Kamhawi, and T. W. Haag, "Facility Effect Characterization Test of NASA's HERMeS Hall Thruster," presented at the 52nd AIAA/SAE/ASEE Joint Propulsion Conference, , Salt Lake City, UT, 2016.

[19] H. Gilland, G. J. Williams, J. M. Burt, and J. Yim, "Carbon Back Sputter Modeling for Hall Thruster Testing," presented at the 52nd AIAA/SAE/ASEE Joint Propulsion Conference, Salt Lake City, UT, 2016.

[20] I. Mikellides, I. Katz, R. Hofer, D. Goebel, K. de Grys, and A. Mathers, "Magnetic Shielding of the Acceleration Channel Walls in a Long-Life Hall Thruster," in *Joint Propulsion Conference, AIAA-10-6942*, Nashville, Tennessee 2010.

[21] I. Mikellides, R. R. Hofer, I. Katz, and D. M. Goebel, "Magnetic Shielding of Hall Thrusters at High Discharge Voltages," *Journal of Applied Physics,* vol. 116, 2013.

[22] H. Kamhawi, D. H. Manzella, T. B. Smith, and G. R. Schmidt, "High-Power Hall Propulsion Development at NASA Glenn Research Center," presented at the Space Propulsion 2012, Bordeaux, France, 2012.

[23] R. R. Hofer, H. Kamhawi, I. Mikellides, D. A. Herman, J. E. Polk, W. Huang*, et al.*, "Design Methodology and Scaling of the 12.5 kW HERMeS Hall Thruster for the Solar Electric Propulsion Technology Demonstration Mission," presented at the Presented at the 62nd JANNAF Propulsion Meeting, Nashville, TN, 2015.

[24] (2016). *NASA GRC Vacuum Facility 5*. Available: https://facilities.grc.nasa.gov/epl/capabilities.html.

[25] J. Yim and J. M. Burt, "Characterization of Vacuum Facility Background Gas Through Simulation and Considerations for Electric Propulsion Ground Testing," in *51st AIAA/SAE/ASEE Joint Propulsion Conference, Propulsion and Energy Forum, AIAA-2015-3825*, Orlando, FL, USA, 2015.

[26] T. W. Haag, "Thrust stand for high-power electric propulsion devices," *Review of Scientific Instruments,* vol. 62, 1991 1991.

[27] T. W. Haag and M. Osborn, "RHETT/EPDM performance characterization," in *International Electric Propulsion Conference, IEPC-97-107*, Cleveland, OH, 1997.

[28] D. L. Brown, R. B. Lobbia, K. D. Hartley, M. Sekerak, D. King, and P. Y. Peterson, "The XR-5 and XR-5A Hall Thrusters, Part 1: Stability and Mode Transitions," in *Joint Army Navy NASA Air Force (JANNAF) conference*, Nashville, TN, 2015.

[29] M. Sekerak, D. L. Brown, R. B. Lobbia, K. D. Hartley, D. King, P. Y. Peterson*, et al.*, "The XR-5 and XR-5A Hall Thrusters, Part 2: Oscillation Behavior," in *Joint Army Navy NASA Air Force (JANNAF) conference*, Nashville, TN, 2015.

[30] H. Kamhawi, W. Huang, T. Haag, and R. Spektor, "Investigation of the Effects of Facility Background Pressure on the Performance and Voltage-Current Characteristics of the High Voltage Hall Accelerator," in *50th AIAA/ASME/SAE/ASEE Joint Propulsion Conference and Exhibit, AIAA-3707-2014*, Cleveland, OH, USA, 2014.

[31] R. Hofer and J. R. Anderson, "Finite Pressure Effects in Magnetically Shielded Hall Thrusters," in *50th AIAA/ASME/SAE/ASEE Joint Propulsion Conference and Exhibit, AIAA-2014-3709*, Cleveland, OH, USA, 2014.